Available online at www.sciencedirect.com
ScienceDirect
Comput. Methods Appl. Mech. Engrg. 394 (2022) 114839
Computer methods in applied mechanics and engineering
www.elsevier.com/locate/cma

A morphoelastic stability framework for post-critical pattern formation in growing thin biomaterials

Rainer M.J. Groh

Bristol Composites Institute, Department of Aerospace Engineering, University of Bristol, UK

Received 22 October 2021; received in revised form 26 January 2022; accepted 4 March 2022
Available online 25 March 2022

Abstract

Morphological instabilities play a key role in the evolution of form and function in growing biomaterials. Spatially varying differential growth, in particular, leads to residual stresses that for soft materials or slender geometries are favourably relieved by out-of-plane buckling or wrinkling. While the onset of instability in growing biomaterials has been studied extensively, the post-critical regime remains poorly understood. To this end, this paper presents a robust computational modelling framework for morphoelastic instabilities and associated post-critical pattern formation. The seven-parameter shell element—commonly used for elasto-plastic analysis of engineering materials—is implemented alongside the multiplicative decomposition of the deformation gradient tensor into a growth and an elastic part. The governing nonlinear equations are solved using a generalised path-following/numerical continuation solver that facilitates comprehensive exploration of the stability landscape through pinpointing of critical points and branch switching at bifurcations. The utility and power of the computational framework is demonstrated by unveiling complex pattern formation phenomena that arise as a result of sequentially occurring morphological instabilities. In particular, we highlight the central role that exponential edge growth plays in fractal wrinkling patterns, the blooming of doubly-curved flower petals, and wavy daffodil trumpets. In addition, the ability of the solver to track critical points through parameter space enables efficient sensitivity studies into the role of material parameters on pattern formation. The presented computational framework is thus a versatile tool for modelling the evolution of form and function in growing biological systems and the design of biotechnology applications.

Keywords: Morphogenesis; Generalised path-following; Instability phenomena; Finite elements

1. Introduction

In morphoelasticity—or the mechanics of elastic growth [1]—instabilities play an important role in the evolution of form and function. Typical examples of morphoelastic instabilities in biological materials include the wrinkling of human skin [2], the rippling of leaves [3,4] and flower petals [5,6], cortical folding in mammalian brains [7,8] and asthmatic airways [9,10], and the formation of channels for liquid transport through biofilms [11,12]. In examples such as cortical folding, malformed instabilities are indicators of disease, and conversely, the sequential pattern formation of a healthy folding pattern is critical for cognitive function [13]. Modelling and controlled experiments of morphoelastic instabilities have therefore attracted increasing research interest, both in understanding the evolution

E-mail address: rainer.groh@bristol.ac.uk.

https://doi.org/10.1016/j.cma.2022.114839

of form and function in biomaterials and in developing new design paradigms for biomimetic technology. An excellent example of biomimetic inspiration is the wrinkling of a stiff, thin film on a compliant substrate [14,15], which has several applications in the development of electronic skins, stretchable electronics [16], and photo-voltaic devices [17].

At the level of the mathematical continuum, growth is often modelled kinematically via the multiplicative decomposition of the deformation gradient tensor into a growth and an elastic part [18,19]. Akin to the modelling of finite-strain thermoelasticity and plasticity, a fictitious intermediate configuration is introduced that represents a stress-free and kinematically incompatible mapping from the initial configuration by means of the growth part of the deformation gradient tensor. The elastic part of the deformation gradient then maps the fictitious intermediate configuration into the deformed and kinematically compatible state, generally leading to internal stresses and stored strain energy. The spatial distribution and temporal evolution of the growth tensor can either be based on phenomenological observations or derived from micromechanical models, and can additionally be coupled to the evolving strains and/or stresses within the material [20]. To describe the elastic behaviour of soft biomaterials, a hyperelastic material model is commonly used (*e.g.*, a Neo-Hookean, Ogden, or Mooney–Rivlin material law, see [21]). As the elastic response of soft materials in the large strain regime is generally volumetrically incompressible, an incompressibility condition is either enforced weakly—resulting in a 'nearly' incompressible approach [22]—or enforced explicitly in a mixed displacement–pressure formulation leading to full incompressibility [23].

The presence of compressive stresses due to differential growth, *i.e.* spatial differences in the freely grown lengths of individual material fibres, can trigger instabilities [24,25] similar to the effect of thermal residual stresses in manufacturing of composite materials [26]. This principle can be exploited for technological applications, where control of an internal growth-like parameter within engineered sheets creates opportunities for embedding target metric tensors [27,28], thereby enabling complex topologies through 'shape programming' [29]. Analytical studies on growth-induced instability phenomena are based on linear eigenvalue analyses that determine the critical growth factor, while asymptotic perturbation approaches are commonly used to model the initial post-bifurcation behaviour, see *e.g.* [7,14,15,24]. Closed-form analytical solutions are invaluable for gaining physical insight, but are usually restricted to simple geometries and boundary conditions. Furthermore, detailed post-bifurcation analyses deep into the post-critical regime, including pattern formation through a sequence of successive instabilities, are usually only possible via dedicated numerical schemes [15].

Due to its geometric versatility, the finite element (FE) method has been a natural candidate to develop computational models of remodelling [30] and growth/atrophy [31,32]. Despite significant progress in developing different FE formulations, the focus has undoubtedly been on two-dimensional planar or three-dimensional solid elements. Since slender and thin-walled geometries in biology, such as plant leaves, flower petals, insect wings, articular cartilages, *etc*., are particularly prone to instabilities by relieving compressive stresses through out-of-plane deformations [33], computational modelling also requires suitable morphoelastic shell elements. Many analytical morphoelastic models have been based on the well-known Föppl–von Kármán (FvK) plate equations [34] with the caveat that the FvK theory is only applicable for moderate deflections/rotations and small strains, *i.e.* a linear constitutive law, although under certain assumptions the model can also be extended to finite-strain hyperelasticity [35]. In the computational domain, Rausch and Kuhl [36] developed a growth model for thin membranes in the commercial FE software ABAQUS CAE through user subroutines. While this model improves computational efficiency by using a two-dimensional reference plane, the model assumes zero through-thickness shear and normal stresses that require a plane-stress reduction of the constitutive tensor, which, in a finite-strain hyperelastic setting, leads to complicated constitutive terms. An advantage of this approach, on the other hand, is that the plane-stress condition can be used to solve for the hydrostatic pressure term that enforces incompressibility. More recently, Zheng et al. [37] developed a morphoelastic solid-shell element that discretises the top and bottom surfaces of the shell rather than using a reference surface. In addition, the solid-shell element by Zheng et al. [37] departs from the framework originally introduced by Himpel et al. [31]. While in Himpel et al. [31] growth is incorporated as an internal variable at integration point level and affects the tangent constitutive tensor, in the approach by Zheng et al. [37] an equivalent growth body force is derived from the objective Truesdell rate.

As an alternative to solid-shell elements, so-called degenerated shell elements—introduced by Ahmad et al. [38]—map a two-dimensional flat master element into a curved three-dimensional surface that represents the mid-plane of the element, see *e.g.* Bischoff et al. [39] for an overview and Büchter and Ramm [40] for a

comparison of degeneration and classical shell theory. Degenerated shell elements approximate the shell mid-surface by interpolating the spatial coordinates of element nodes using shape functions, and describe the shell thickness by a unit vector at each node (the shell director) that is initially perpendicular to the shell mid-surface and rotates alongside the deforming mid-surface. The degenerated shell formulation is then completed by postulating appropriate kinematic assumptions on the displacement field. For example, five-parameter shell elements use three Cartesian displacements per node and parametrise the rotation of the shell director using two rotation variables. In these five-parameter models, thickness stretch is neglected (first-order shear deformation theory [41]) such that the plane-stress assumption must be imposed on the constitutive tensor. Furthermore, the inextensibility of the shell director needs to be enforced exactly throughout the finite deformation process, and this is conveniently achieved using a rotation tensor, for example, through the exponential map [42]. In contrast, six-parameter formulations allow for thickness stretch and therefore use the full three-dimensional constitutive equations with an additive update of the shell director using a difference vector [43]. However, the six-parameter shell suffers from so-called 'Poisson thickness locking' [44]. In bending-dominated problems the linear distribution of the transverse normal stress through the thickness of the shell—caused by Poisson's action of the linear through-thickness variation of the in-plane strains—is not balanced by the kinematically assumed state of constant transverse normal strain.

To overcome Poisson's locking in the six-parameter formulation, the transverse displacement is enhanced by an additional seventh parameter that results in a quadratic through-thickness displacement field and an ensuing linear distribution of the transverse normal strain. Since the initial work by Büchter and Ramm [45], the seven-parameter shell formulation has been shown to be the transverse shear and transverse normal deformable shell model with the fewest degrees of freedom that works robustly with full three-dimensional constitutive laws [46]. Beyond Poisson's locking, it is well known that low p-refinement shell elements (*e.g.* linear and quadratic elements) suffer from locking phenomena (*e.g.* transverse shear and membrane locking) when formulated entirely in a displacement-based manner. To overcome the artificial stiffening in low-order finite elements, mixed variational principles can be employed to develop locking-free formulations with effective examples being the assumed natural strain [47] and enhanced assumed strain [48] concepts. Alternatively, higher-order shell elements with sufficient p-refinement have also been shown to provide reliable and efficient locking-free solutions using a purely displacement-based formulation, both for classical Lagrangian [49] and NURBS-based [50] shape functions.

In this paper, a seven-parameter quadrilateral shell element is developed for the analysis of growth-induced instability phenomena in slender biomaterials and structures. Growth is modelled via the multiplicative decomposition of the deformation gradient tensor into a growth and an elastic part with the growth factor imposed at integration point level. A 'nearly' incompressible Neo-Hookean material model is implemented leading to an entirely displacement-based formulation. Shear and membrane locking are practically eliminated through higher-order spectral/hp-refinement following Payette and Reddy [49] with full numerical integration of all quantities. An additional advantage of high p-refinement is that it overcomes the poor performance of low-order elements in a morphoelastic setting [23,51].

The main novelty of the paper is the robust post-critical analysis of morphoelastic instability phenomena through extended solver functionality, *e.g.* pinpointing of critical points, branch switching at bifurcations, and multi-parametric explorations of the stability landscape. Previous work has employed small manually-prescribed force or displacement perturbations [52] to bias the solver towards one branch of a bifurcation, but this method is sensitive to the perturbation size, requires preliminary insight into the problem, and precludes a comprehensive exploration of the equilibrium manifold. More recently, eigenvalue tracking has been used on non-perturbed models to pinpoint critical growth factors more accurately using bisection [51]. A more efficient and robust method is to pinpoint instability points directly using an extended system that enforces the criticality condition [53].

The present paper departs from the current literature in that the combination of an efficient shell element with robust numerical continuation algorithms enables the comprehensive exploration of sequential bifurcation events as well as growth-mediated pattern formation in the post-critical regime. This valuable capability is illustrated through a number of pertinent examples on growing biomaterials that feature exponential edge growth and is also used to explore the effect of different material models on the observed post-critical pattern formation. Indeed, an efficient exploration of the parametric variation of critical growth rates and their associated buckling patterns can be traced by path-following the locus of the critical point through parameter space. This capability is especially useful in a biological setting, where material properties and/or geometrical dimensions are often uncertain, as well as in biomimetic technology development, where critical point tracking enables rapid design iteration.

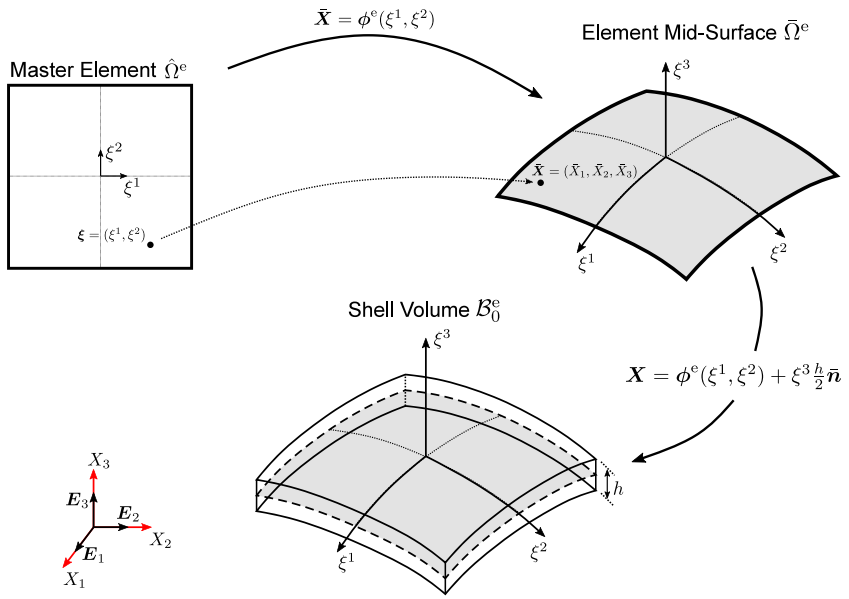

Fig. 1. Modelling the geometry of a 3D shell patch in the undeformed, reference configuration using (i) an isoparametric map from a master element defined on the unit square to an FE approximation of the shell mid-surface, followed by (ii) an additional linear mapping that constructs the shell volume by extending the shell thickness in the direction of the normal vector.

In summary, this paper couples a morphoelastic seven-parameter shell element to a generalised path-following/numerical continuation solver to develop a robust framework for modelling growth-induced instability phenomena. Section 2 covers the theory of the developed shell element, while Section 3 introduces the generalised path-following solver. In Section 4, the stability framework is validated using literature benchmarks and applied to exponential edge growth in leaves (including fractal wrinkling patterns), the folding of a daffodil's corona, and the blooming of doubly-curved flower petals. Section 5 then studies the effect of different material models on the observed results. Finally, conclusions are drawn in Section 6.

2. Morphoelastic seven-parameter shell element

This section first outlines the general formulation of the seven-parameter shell element, and then develops this model in the framework of morphoelastic kinematics based on the multiplicative decomposition of the deformation gradient and a 'nearly' incompressible hyperelastic material law. The weak form of the equilibrium equation is then discretised using higher-order polynomial (p-refined) shape functions based on a Chebychev–Gauss–Lobatto grid.

2.1. Definition of the undeformed shell mid-surface

A shell structure is generally defined as a 3D body with one dimension (the thickness) significantly smaller than the other two (in-plane) dimensions. In contrast to membranes, shells resist external loads by both membrane and bending stresses. In classical shell theory, the 3D solid body is decomposed into a 2D reference surface $\Omega \subset \mathbb{R}^3$, oftentimes the undeformed mid-surface of the shell, and a normal vector $\boldsymbol{n}$ with an associated shell thickness h. Here, Ω is approximated by an interpolated surface $\bar{\Omega}$ comprising a set of N_e higher-order quadrilateral finite elements, *i.e.* $\bar{\Omega} = \cup_{e=1}^{N_e} \bar{\Omega}^e$, with each node of $\bar{\Omega}^e$ lying on the reference surface Ω. Each finite element surface $\bar{\Omega}^e$ is defined via the master element $\hat{\Omega}^e = [-1, 1]^2$ with $\xi^1 \in [-1, 1]$ and $\xi^2 \in [-1, 1]$ acting as the two local coordinates of $\hat{\Omega}^e$. Hence, we have an injective mapping $\boldsymbol{\phi}^e(\xi_1, \xi_2) : \hat{\Omega}^e \to \bar{\Omega}^e \subset \mathbb{R}^3$ (see Fig. 1).

The reference surface $\bar{\Omega}^e$ of each seven-parameter shell element is chosen to lie on the undeformed shell mid-surface and is interpolated using 2D isoparametric shape functions ψ_k from the nodal coordinates $\bar{\boldsymbol{X}}^k$, with k

indicating the node index number:

$$\bar{\boldsymbol{X}} = \boldsymbol{\phi}^{\mathrm{e}}(\xi^1, \xi^2) = \sum_{k=1}^{N_{\mathrm{n}}} \psi_k(\xi^1, \xi^2)\bar{\boldsymbol{X}}^k \quad \text{where} \quad (\xi^1, \xi^2) \in \hat{\Omega}^{\mathrm{e}}. \tag{1}$$

Hence, the coordinates $\bar{\boldsymbol{X}}$ of any point on the mid-surface of the shell falling within the eth element are interpolated from the element nodal coordinates $\bar{\boldsymbol{X}}^k = \bar{X}_i^k \boldsymbol{E}_i$,[1] where $\{\boldsymbol{E}_1, \boldsymbol{E}_2, \boldsymbol{E}_3\}$ are the basis vectors of a fixed global Cartesian coordinate system. Indeed, all further nodal quantities, such as the displacement and difference vector introduced later, are described in relation to this global Cartesian coordinate frame.

To complete the geometric description of the mid-surface we define the covariant basis vectors

$$\bar{\boldsymbol{g}}_\alpha(\xi^1, \xi^2) = \frac{\partial \bar{\boldsymbol{X}}}{\partial \xi^\alpha} = \sum_{k=1}^{N_{\mathrm{n}}} \frac{\partial \psi_k(\xi^1, \xi^2)}{\partial \xi^\alpha} \bar{\boldsymbol{X}}^k \tag{2}$$

at each point of the discretised mid-surface $\bar{\Omega}^{\mathrm{e}}$. The two pointwise vectors $\bar{\boldsymbol{g}}_\alpha$ are tangent to the mid-surface plane and are therefore used to define a unit normal vector at each point of the mid-surface:

$$\bar{\boldsymbol{n}}(\xi^1, \xi^2) = \frac{\bar{\boldsymbol{g}}_1 \times \bar{\boldsymbol{g}}_2}{\|\bar{\boldsymbol{g}}_1 \times \bar{\boldsymbol{g}}_2\|_2}. \tag{3}$$

Hence, for each coordinate $(\xi^1, \xi^2) \in \hat{\Omega}^{\mathrm{e}}$, the vectors $\{\bar{\boldsymbol{g}}_1, \bar{\boldsymbol{g}}_2, \bar{\boldsymbol{n}}\}$ define a basis for $\mathbb{R}^3$.

The undeformed volume of an elemental portion of the shell $\mathcal{B}_0^{\mathrm{e}}$ is now constructed by extending the mid-surface in the direction of the mid-surface normal $\bar{\boldsymbol{n}}$ using the coordinate $\xi^3 \in [-1, 1]$. For a shell element with local thickness h, nodal thickness value h_k, and nodal normal vector $\bar{\boldsymbol{n}}^k$ we have:

$$\boldsymbol{X} = \boldsymbol{\Phi}^{\mathrm{e}}(\xi^1, \xi^2, \xi^3) = \boldsymbol{\phi}^{\mathrm{e}}(\xi^1, \xi^2) + \xi^3 \frac{h}{2} \bar{\boldsymbol{n}}(\xi^1, \xi^2) = \sum_{k=1}^{N_{\mathrm{n}}} \psi_k(\xi^1, \xi^2) \left(\bar{\boldsymbol{X}}^k + \xi^3 \frac{h_k}{2} \bar{\boldsymbol{n}}^k \right). \tag{4}$$

The sequence of steps mapping the master element $\hat{\Omega}^{\mathrm{e}}$ into the shell volume $\mathcal{B}_0^{\mathrm{e}}$ is shown in Fig. 1.

For each point in the shell volume $\mathcal{B}_0^{\mathrm{e}}$, not necessarily on the mid-surface $\bar{\Omega}^{\mathrm{e}}$, we can now define covariant basis vectors

$$\boldsymbol{g}_i(\xi^1, \xi^2, \xi^3) = \frac{\partial \boldsymbol{X}}{\partial \xi^i} = \sum_{k=1}^{N_{\mathrm{n}}} \frac{\partial}{\partial \xi^i} \left[\psi_k(\xi^1, \xi^2) \left(\bar{\boldsymbol{X}}^k + \xi^3 \frac{h_k}{2} \bar{\boldsymbol{n}}^k \right) \right]. \tag{5}$$

Using the covariant basis vectors of the mid-surface in Eq. (2) we can write

$$\boldsymbol{g}_\alpha = \bar{\boldsymbol{g}}_\alpha + \xi^3 \frac{h}{2} \bar{\boldsymbol{n}}_{,\alpha} = \sum_{k=1}^{N_{\mathrm{n}}} \frac{\partial \psi_k(\xi^1, \xi^2)}{\partial \xi^\alpha} \left(\bar{\boldsymbol{X}}^k + \xi^3 \frac{h_k}{2} \bar{\boldsymbol{n}}^k \right), \tag{6a}$$

$$\boldsymbol{g}_3 = \frac{h}{2} \bar{\boldsymbol{n}} = \sum_{k=1}^{N_{\mathrm{n}}} \psi_k(\xi^1, \xi^2) \frac{h_k}{2} \bar{\boldsymbol{n}}^k. \tag{6b}$$

The dual or contravariant basis vectors $\boldsymbol{g}^i$ are defined by the relation $\boldsymbol{g}^i \cdot \boldsymbol{g}_j = \delta^i_j$, where δ^i_j is the Kronecker delta. The covariant and contravariant basis vectors are conveniently used in the element formulation for all tensorial quantities, and the volume integrals that appear in the weak form of the equilibrium equation are computed over the curvilinear coordinates (ξ^1, ξ^2, ξ^3).

To complete the geometrical description we consider a differential line element

$$\mathrm{d}\boldsymbol{X} = \boldsymbol{g}_1 \mathrm{d}\xi^1 + \boldsymbol{g}_2 \mathrm{d}\xi^2 + \boldsymbol{g}_3 \mathrm{d}\xi^3 \tag{7}$$

[1] Throughout the paper, Einstein summation is implied over repeated indices. Furthermore, Greek indices range over 1 and 2 and Latin indices range over 1, 2, and 3.

in the undeformed body $\mathcal{B}_0^{\mathrm{e}}$.[2] In matrix–vector notation

$$\begin{pmatrix} \mathrm{d}X_1 \\ \mathrm{d}X_2 \\ \mathrm{d}X_3 \end{pmatrix} = \begin{bmatrix} \frac{\partial X_1}{\partial \xi^1} & \frac{\partial X_1}{\partial \xi^2} & \frac{\partial X_1}{\partial \xi^3} \\ \frac{\partial X_2}{\partial \xi^1} & \frac{\partial X_2}{\partial \xi^2} & \frac{\partial X_2}{\partial \xi^3} \\ \frac{\partial X_3}{\partial \xi^1} & \frac{\partial X_3}{\partial \xi^2} & \frac{\partial X_3}{\partial \xi^3} \end{bmatrix} \begin{pmatrix} \mathrm{d}\xi^1 \\ \mathrm{d}\xi^2 \\ \mathrm{d}\xi^3 \end{pmatrix} = [J]\{\mathrm{d}\xi\}, \tag{8}$$

where $[J]$ is the Jacobian matrix and the determinant of $[J]$ is J. Using the determinant J, the differential volume element is $\mathrm{d}V_0 = J\mathrm{d}\xi^1\mathrm{d}\xi^2\mathrm{d}\xi^3$. Similarly, the length squared of the differential line element is

$$\mathrm{d}\boldsymbol{X} \cdot \mathrm{d}\boldsymbol{X} = \left(\boldsymbol{g}_i \cdot \boldsymbol{g}_j\right) \mathrm{d}\xi^i \mathrm{d}\xi^j = G_{ij}\mathrm{d}\xi^i\mathrm{d}\xi^j, \tag{9}$$

where $G_{ij} = \boldsymbol{g}_i \cdot \boldsymbol{g}_j$ are the covariant components of the metric tensor $\boldsymbol{G}$, *i.e.* $\boldsymbol{G} = G_{ij}\boldsymbol{g}^i \otimes \boldsymbol{g}^j$. The contravariant components G^{ij} of the metric tensor are given by $[G^{ij}] = [G_{ij}]^{-1}$, and this allows the contravariant basis vectors $\boldsymbol{g}^i$ to be computed as follows

$$\boldsymbol{g}^i = G^{ij}\boldsymbol{g}_j. \tag{10}$$

2.2. Axiomatic displacement field

The original, undeformed configuration of each shell element $\mathcal{B}_0^{\mathrm{e}}$ is now mapped into a new configuration $\mathcal{B}_t^{\mathrm{e}}$ at time t via the conformal map $\boldsymbol{\chi}(\boldsymbol{X}, t)$. Thus, each material point with position vector $\boldsymbol{X}$ in the original configuration moves to a new position vector $\boldsymbol{x} = \boldsymbol{\chi}(\boldsymbol{X}, t)$. The displacement of each material point at time t is

$$\boldsymbol{u}(\boldsymbol{X}, t) = \boldsymbol{\chi}(\boldsymbol{X}, t) - \boldsymbol{X} = \boldsymbol{x} - \boldsymbol{X}.$$

Following the assumptions of the seven-parameter shell model [46,49], the displacement vector is expanded as a quadratic function in the shell thickness direction (coordinate ξ^3). This assumption guarantees that the resulting shell model is asymptotically consistent with 3D elasticity and therefore facilitates the use of the full 3D constitutive tensor without plane strain or plane stress assumptions in the thickness direction. The seven-parameter expansion of the displacement vector reads

$$\boldsymbol{u}(\xi^1, \xi^2, \xi^3) = \boldsymbol{v}(\xi^1, \xi^2) + \xi^3 \frac{h}{2}\boldsymbol{w}(\xi^1, \xi^2) + \left(\xi^3\right)^2 \frac{h}{2}\boldsymbol{\Psi}(\xi^1, \xi^2), \tag{11}$$

where the time variable t is henceforth omitted for brevity. The vector $\boldsymbol{v}(\xi^1, \xi^2) = v_i(\xi^1, \xi^2)\boldsymbol{E}_i$ represents the mid-surface displacement vector and the vector $\boldsymbol{w}(\xi^1, \xi^2) = w_i(\xi^1, \xi^2)\boldsymbol{E}_i$ is the so-called *difference* vector that describes the vectorial change of the original mid-surface normal vector $\bar{\boldsymbol{n}}$. The vector $\boldsymbol{\Psi}(\xi^1, \xi^2) = \Psi(\xi^1, \xi^2)\bar{\boldsymbol{n}}(\xi^1, \xi^2)$ is a function of the scalar parameter $\Psi(\xi^1, \xi^2)$ also defined on the shell mid-surface, and this seventh parameter prevents the spurious phenomenon of Poisson's locking present in the six-parameter formulation (see Section 1).

The position vector of each material point in the current configuration is thus

$$\boldsymbol{x}(\xi^1, \xi^2, \xi^3) = \boldsymbol{X} + \boldsymbol{u} = \bar{\boldsymbol{x}}(\xi^1, \xi^2) + \xi^3 \frac{h}{2}\bar{\boldsymbol{d}}(\xi^1, \xi^2) + \left(\xi^3\right)^2 \frac{h}{2}\Psi(\xi^1, \xi^2)\bar{\boldsymbol{n}}(\xi^1, \xi^2) \tag{12}$$

with $\bar{\boldsymbol{x}} = \bar{\boldsymbol{X}} + \boldsymbol{v}$ being the position vector of the deformed shell mid-surface, and $\bar{\boldsymbol{d}} = \bar{\boldsymbol{n}} + \boldsymbol{w}$ being the deformed shell director vector (not necessarily normal to the deformed shell mid-surface, nor necessarily of unit length).

The finite element interpolation of the displacement field in Eq. (11) is given by

$$\boldsymbol{u}(\xi^1, \xi^2, \xi^3) = \sum_{k=1}^{N_{\mathrm{n}}} \psi_k(\xi^1, \xi^2) \left[\boldsymbol{v}^k + \xi^3 \frac{h_k}{2}\boldsymbol{w}^k + \left(\xi^3\right)^2 \Psi^k \sum_{l=1}^{N_{\mathrm{n}}} \psi_l(\xi^1, \xi^2) \frac{h_l}{2}\bar{\boldsymbol{n}}^l \right]. \tag{13}$$

Note that in the final term the two components of $\boldsymbol{\Psi}(\xi^1, \xi^2) = \Psi(\xi^1, \xi^2)\bar{\boldsymbol{n}}(\xi^1, \xi^2)$ are interpolated separately and not as a single item. This means the derivatives of the displacement field with respect to the curvilinear coordinates, (ξ^1, ξ^2, ξ^3), are

$$\boldsymbol{u}_{,\alpha} = \sum_{k=1}^{N_{\mathrm{n}}} \frac{\partial \psi_k(\xi^1, \xi^2)}{\partial \xi^\alpha} \left[\boldsymbol{v}^k + \xi^3 \frac{h_k}{2}\boldsymbol{w}^k + \left(\xi^3\right)^2 \left(\Psi^k \sum_{l=1}^{N_{\mathrm{n}}} \psi_l(\xi^1, \xi^2) \frac{h_l}{2}\bar{\boldsymbol{n}}^l + \frac{h_k}{2}\bar{\boldsymbol{n}}^k \sum_{l=1}^{N_{\mathrm{n}}} \psi_l(\xi^1, \xi^2)\, \Psi^l \right) \right] \tag{14a}$$

[2] A total Lagrangian formulation with integrals computer over the undeformed configuration is used herein.

$$\boldsymbol{u}_{,3} = \sum_{k=1}^{N_\mathrm{n}} \psi_k(\xi^1,\xi^2)\left(\frac{h_k}{2}\boldsymbol{w}^k + \xi^3\,\Psi^k \sum_{l=1}^{N_\mathrm{n}} \psi_l(\xi^1,\xi^2) h_l \bar{\boldsymbol{n}}^l\right). \tag{14b}$$

For each point in the deformed shell volume $\mathcal{B}_t^\mathrm{e}$, we now have a new set of covariant basis vectors

$$\boldsymbol{h}_i(\xi^1,\xi^2,\xi^3) = \frac{\partial \boldsymbol{x}}{\partial \xi^i} = \frac{\partial \boldsymbol{X}}{\partial \xi^i} + \frac{\partial \boldsymbol{u}}{\partial \xi^i} = \boldsymbol{g}_i + \boldsymbol{u}_{,i}, \tag{15}$$

which are used to compute the deformation gradient tensor

$$\boldsymbol{F} = \frac{\partial \boldsymbol{x}}{\partial \boldsymbol{X}} = \frac{\partial \boldsymbol{x}}{\partial \xi^i} \otimes \frac{\partial \xi^i}{\partial \boldsymbol{X}} = \boldsymbol{h}_i \otimes \boldsymbol{g}^i. \tag{16}$$

In combination with the identity tensor $\boldsymbol{I}$, the Green–Lagrange strain tensor is then given by

$$\boldsymbol{E} = \frac{1}{2}\left(\boldsymbol{F}^\top \boldsymbol{F} - \boldsymbol{I}\right) = \frac{1}{2}\left[\left(\boldsymbol{g}^i \otimes \boldsymbol{h}_i\right)\left(\boldsymbol{h}_j \otimes \boldsymbol{g}^j\right) - \boldsymbol{g}_i \otimes \boldsymbol{g}^i\right] = \frac{1}{2}\left[\boldsymbol{h}_i \cdot \boldsymbol{h}_j - \boldsymbol{g}_i \cdot \boldsymbol{g}_j\right] \boldsymbol{g}^i \otimes \boldsymbol{g}^j, \tag{17}$$

with covariant components $E_{ij} = \frac{1}{2}\left(H_{ij} - G_{ij}\right)$ and $H_{ij} = \boldsymbol{h}_i \cdot \boldsymbol{h}_j$ and $G_{ij} = \boldsymbol{g}_i \cdot \boldsymbol{g}_j$. The covariant coefficients E_{ij} are now expanded in terms of the through-thickness coordinate ξ^3:

$$E_{ij}(\xi^1,\xi^2,\xi^3) = \underline{\epsilon_{ij}(\xi^1,\xi^2) + \xi^3 \kappa_{ij}(\xi^1,\xi^2)} + \left(\xi^3\right)^2 \gamma_{ij}(\xi^1,\xi^2) + \left(\xi^3\right)^3 \eta_{ij}(\xi^1,\xi^2) + \left(\xi^3\right)^4 \rho_{ij}(\xi^1,\xi^2). \tag{18}$$

To make the shell formulation consistent with a first-order shear and normal deformable theory, we only retain the underlined parts of Eq. (18). These are given by:

$$\epsilon_{\alpha\beta} = \frac{1}{2}\left(\boldsymbol{v}_{,\alpha} \cdot \bar{\boldsymbol{g}}_\beta + \bar{\boldsymbol{g}}_\alpha \cdot \boldsymbol{v}_{,\beta} + \boldsymbol{v}_{,\alpha} \cdot \boldsymbol{v}_{,\beta}\right) \tag{19a}$$

$$\kappa_{\alpha\beta} = \frac{h}{4}\left[\boldsymbol{v}_{,\alpha} \cdot \left(\bar{\boldsymbol{n}}_{,\beta} + \boldsymbol{w}_{,\beta}\right) + \left(\bar{\boldsymbol{n}}_{,\alpha} + \boldsymbol{w}_{,\alpha}\right) \cdot \boldsymbol{v}_{,\beta} + \boldsymbol{w}_{,\alpha} \cdot \bar{\boldsymbol{g}}_\beta + \bar{\boldsymbol{g}}_\alpha \cdot \boldsymbol{w}_{,\beta}\right] \tag{19b}$$

$$\epsilon_{\alpha 3} = \frac{h}{4}\left[\boldsymbol{v}_{,\alpha} \cdot \left(\bar{\boldsymbol{n}} + \boldsymbol{w}\right) + \bar{\boldsymbol{g}}_\alpha \cdot \boldsymbol{w}\right] \tag{19c}$$

$$\kappa_{\alpha 3} = \frac{h^2}{8}\left[\boldsymbol{w}_{,\alpha} \cdot \bar{\boldsymbol{n}} + \left(\bar{\boldsymbol{n}}_{,\alpha} + \boldsymbol{w}_{,\alpha}\right) \cdot \boldsymbol{w}\right] + \frac{h}{2}\left(\bar{\boldsymbol{g}}_\alpha + \boldsymbol{v}_{,\alpha}\right) \cdot \boldsymbol{\Psi} \tag{19d}$$

$$\epsilon_{33} = \frac{h^2}{8}\left(2\bar{\boldsymbol{n}} + \boldsymbol{w}\right) \cdot \boldsymbol{w} \tag{19e}$$

$$\kappa_{33} = \frac{h^2}{2}\left(\bar{\boldsymbol{n}} + \boldsymbol{w}\right) \cdot \boldsymbol{\Psi}. \tag{19f}$$

The inconsistency of the six-parameter shell formulation becomes apparent when we enforce $\boldsymbol{\Psi} = \boldsymbol{0}$, in which case the term accounting for the linear variation of the through-thickness strain vanishes, *i.e.* $\kappa_{33} = 0$.

2.3. Growth kinematics

To introduce the kinematics of growth, the deformation gradient tensor at time t is decomposed in a multiplicative fashion [18] as follows

$$\boldsymbol{F} = \boldsymbol{F}_\mathrm{e} \boldsymbol{F}_\mathrm{g}, \tag{20}$$

where $\boldsymbol{F}_\mathrm{e}$ is the elastic deformation tensor defined in a fictitious and intermediate, stress-free configuration $\mathcal{B}_g$. Hence, $\boldsymbol{F}_\mathrm{e}$ maps a differential line element $\mathrm{d}\hat{\boldsymbol{X}}$ from the intermediate, stress-free configuration $\mathcal{B}_g$ into the differential line element $\mathrm{d}\boldsymbol{x}$ in the stressed configuration $\mathcal{B}_t$. In addition, the growth tensor $\boldsymbol{F}_\mathrm{g}$ maps a differential line element $\mathrm{d}\boldsymbol{X}$ from the original, undeformed configuration $\mathcal{B}_0$ into the intermediate configuration $\mathcal{B}_g$. As shown in Fig. 2, the multiplicative decomposition accounts for stress-free and kinematically incompatible growth of a body into an intermediate, fictitious state followed by additional elastic and stress-inducing deformations that ensure geometric compatibility. In this process it is assumed that the density of the growing body remains constant ($\rho_0 = \rho_g = \rho_t$) such that any change in mass leads to a change in volume. By assuming that all elastic deformations from $\mathcal{B}_g$ to $\mathcal{B}_t$ are incompressible, we have $J_\mathrm{e} = \det \boldsymbol{F}_\mathrm{e} = 1$ and $J = \det \boldsymbol{F} = \det \boldsymbol{F}_\mathrm{g} = J_\mathrm{g}$.

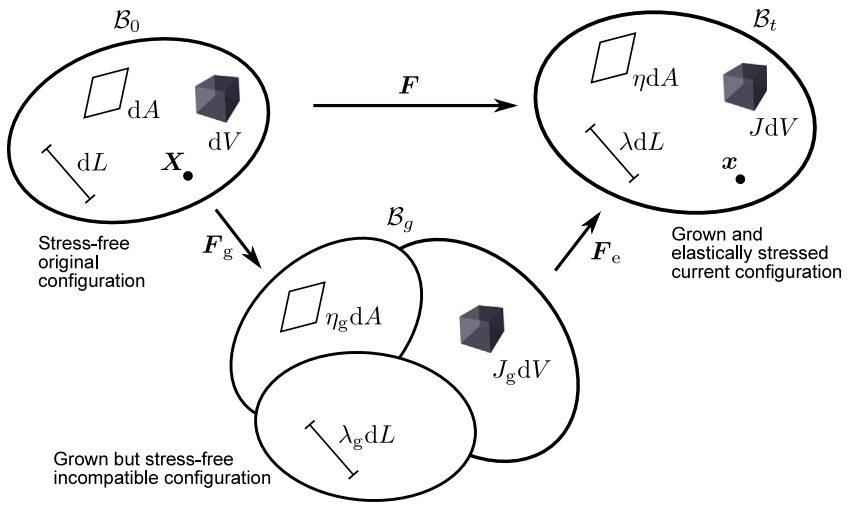

Fig. 2. Growth kinematics represented by a multiplicative decomposition of the deformation gradient tensor $\boldsymbol{F} = \boldsymbol{F}_\mathrm{e}\boldsymbol{F}_\mathrm{g}$ into a growth tensor $\boldsymbol{F}_\mathrm{g}$ and an elastic deformation $\boldsymbol{F}_\mathrm{e}$. The symbols (λ, η, J) represent scaled line, area, and volumetric dimensions.

With the multiplicative decomposition of the deformation gradient tensor in Eq. (20), the Green–Lagrange strain tensor of Eq. (17) can be decomposed into

$$\boldsymbol{E} = \frac{1}{2}\left(\boldsymbol{F}^\top\boldsymbol{F} - \boldsymbol{I}\right) = \boldsymbol{E}_\mathrm{g} + \boldsymbol{F}_\mathrm{g}^\top\boldsymbol{E}_\mathrm{e}\boldsymbol{F}_\mathrm{g}, \tag{21}$$

with the elastic and growth strain tensors defined as

$$\boldsymbol{E}_\mathrm{g} = \frac{1}{2}\left(\boldsymbol{F}_\mathrm{g}^\top\boldsymbol{F}_\mathrm{g} - \boldsymbol{I}\right) \quad \text{and} \quad \boldsymbol{E}_\mathrm{e} = \frac{1}{2}\left(\boldsymbol{F}_\mathrm{e}^\top\boldsymbol{F}_\mathrm{e} - \boldsymbol{I}\right). \tag{22}$$

Eq. (22) shows that $\boldsymbol{E}_\mathrm{g}$ is the Green–Lagrange strain with respect to the original, undeformed configuration as a result of free and unconstrained growth. The term $\boldsymbol{E}_\mathrm{e}$ is an incremental Green–Lagrange strain due to the elastic deformations with the intermediate, stress-free state as the reference configuration. Eq. (21) then pulls $\boldsymbol{E}_\mathrm{e}$ back to the original, undeformed configuration via $\boldsymbol{F}_\mathrm{g}$ and adds it to $\boldsymbol{E}_\mathrm{g}$ to give the total Green–Lagrange strain $\boldsymbol{E}$ with respect to the undeformed configuration.

In an analysis, the growth tensor $\boldsymbol{F}_\mathrm{g}$ is generally specified via an assumed growth law for which the associated equilibrium state is then computed. For example, we might specify $\boldsymbol{F}_\mathrm{g} = F_{\mathrm{g},ij}(\lambda_\mathrm{g})\boldsymbol{E}_i \otimes \boldsymbol{E}_j$, where λ_g is a scalar parameter that controls growth in the Cartesian coordinate system $\{\boldsymbol{E}_1, \boldsymbol{E}_2, \boldsymbol{E}_3\}$. For each iteration of an incremental-iterative solution process, the terms $\boldsymbol{F}$ and $\boldsymbol{E}$ can be computed from the current displacement field, and $\boldsymbol{F}_\mathrm{e}$ and $\boldsymbol{E}_\mathrm{e}$ can then be back-calculated using Eqs (21) and (22).

2.4. Hyperelastic constitutive law accounting for growth

Following Lubarda and Hoger [54] and Ben Amar and Goriely [24], the strain energy density of a growing body is given by

$$\hat{W} = J_\mathrm{g}W, \tag{23}$$

where W is the strain energy density function for elastic deformations from $\mathcal{B}_g$ to $\mathcal{B}_t$ and multiplication by J_g accounts for the increase in volume due to growth from $\mathcal{B}_0$ to $\mathcal{B}_g$. In this paper, a 'nearly' incompressible hyperelastic Neo-Hookean material law is used, but other nonlinear constitutive models can equally be applied with the morphoelastic seven-parameter shell element (see Section 5). Using the 'nearly' incompressible Neo-Hookean law defined in Wriggers [22], modified for material growth following Zheng et al. [37], we write

$$\hat{W} = \frac{\mu}{2}J_\mathrm{g}\left(J_\mathrm{e}^{-\frac{2}{3}}\mathrm{tr}\boldsymbol{C}_\mathrm{e} - 3\right) + \frac{K}{2}\left(J_\mathrm{e} - 1\right)^2, \tag{24}$$

where $\boldsymbol{C}_\mathrm{e} = \boldsymbol{F}_\mathrm{e}^\top \boldsymbol{F}_\mathrm{e} = 2\boldsymbol{E}_\mathrm{e} + \boldsymbol{I}$ is the elastic right Cauchy–Green deformation tensor, μ is the shear modulus, and K is the bulk modulus of the material. Thus, only elastic deformations from $\mathcal{B}_g$ to $\mathcal{B}_t$, represented by $\boldsymbol{C}_\mathrm{e}$, store strain energy and the incompressibility condition is enforced weakly by $K \gg \mu$.

The elastic second Piola–Kirchhoff stress is computed via the usual differentiation of the strain energy density with respect to the Green–Lagrange strain $\boldsymbol{E}$ (or alternatively the right Cauchy–Green deformation tensor $\boldsymbol{C} = \boldsymbol{F}^\top \boldsymbol{F} = 2\boldsymbol{E} + \boldsymbol{I}$):

$$\boldsymbol{S} = \frac{\partial \hat{W}}{\partial \boldsymbol{E}} \equiv 2\frac{\partial \hat{W}}{\partial \boldsymbol{C}} = 2\frac{\partial \hat{W}}{\partial \boldsymbol{C}_\mathrm{e}} : \frac{\partial \boldsymbol{C}_\mathrm{e}}{\partial \boldsymbol{C}} = \boldsymbol{S}_\mathrm{e} : \frac{\partial \boldsymbol{C}_\mathrm{e}}{\partial \boldsymbol{C}}. \tag{25}$$

As the growth strain tensor $\boldsymbol{E}_\mathrm{g}$ does not lead to stored strain energy, the derivative $\frac{\partial \hat{W}}{\partial \boldsymbol{E}_\mathrm{e}} = 2\frac{\partial \hat{W}}{\partial \boldsymbol{C}_\mathrm{e}}$ is the elastic second Piola–Kirchhoff stress tensor $\boldsymbol{S}_\mathrm{e}$ defined with respect to the intermediate configuration. From the definition of $\boldsymbol{C} = \boldsymbol{F}^\top \boldsymbol{F}$ and the multiplicative decomposition $\boldsymbol{F} = \boldsymbol{F}_\mathrm{e}\boldsymbol{F}_\mathrm{g}$, we obtain $\boldsymbol{C} = \boldsymbol{F}_\mathrm{g}^\top \boldsymbol{C}_\mathrm{e} \boldsymbol{F}_\mathrm{g}$ such that in global Cartesian coordinates $\frac{\partial \boldsymbol{C}_\mathrm{e}}{\partial \boldsymbol{C}} = F^{-\top}_{\mathrm{g},ik} F^{-1}_{\mathrm{g},lj} \boldsymbol{E}_i \otimes \boldsymbol{E}_j \otimes \boldsymbol{E}_k \otimes \boldsymbol{E}_l$. By substituting this derivative into Eq. (25), the second Piola–Kirchhoff stress defined with respect to the original, undeformed configuration is given by

$$\boldsymbol{S} = \boldsymbol{F}_\mathrm{g}^{-1} \boldsymbol{S}_\mathrm{e} \boldsymbol{F}_\mathrm{g}^{-\top}. \tag{26}$$

For the material law in Eq. (24), the elastic second Piola–Kirchhoff stress tensor is

$$\begin{aligned} \boldsymbol{S}_\mathrm{e} &= \mu J_\mathrm{g} \left[\frac{\partial J_\mathrm{e}^{-\frac{2}{3}}}{\partial \boldsymbol{C}_\mathrm{e}} (\mathrm{tr}\boldsymbol{C}_\mathrm{e}) + J_\mathrm{e}^{-\frac{2}{3}} \frac{\partial (\mathrm{tr}\boldsymbol{C}_\mathrm{e})}{\partial \boldsymbol{C}_\mathrm{e}} \right] + 2K\,(J_\mathrm{e} - 1)\,\frac{\partial J_\mathrm{e}}{\partial \boldsymbol{C}_\mathrm{e}} \\ &= \mu J_\mathrm{g} J_\mathrm{e}^{-\frac{2}{3}} \left[\boldsymbol{I} - \frac{1}{3}\,(\mathrm{tr}\boldsymbol{C}_\mathrm{e})\,\boldsymbol{C}_\mathrm{e}^{-1} \right] + K J_\mathrm{e}\,(J_\mathrm{e} - 1)\,\boldsymbol{C}_\mathrm{e}^{-1}, \end{aligned} \tag{27}$$

from which $\boldsymbol{S}$ can be computed via Eq. (26) for the defined growth tensor $\boldsymbol{F}_\mathrm{g}$. In the variational form of the equilibrium statement (see Section 2.5), the contravariant components of the second Piola–Kirchhoff stress S^{ij} in the covariant shell basis $\{\boldsymbol{g}_1, \boldsymbol{g}_2, \boldsymbol{g}_3\}$ are used in combination with the covariant components of the Green–Lagrange strain E_{ij} in the contravariant shell basis $\{\boldsymbol{g}^1, \boldsymbol{g}^2, \boldsymbol{g}^3\}$. In this case, the indicial form of Eq. (26) reads

$$S^{ij} = F_\mathrm{g}^{-1,ik} S_{\mathrm{e},kl} F_\mathrm{g}^{-1,jl} \tag{28}$$

where $F_\mathrm{g}^{-1,ij}$ are the contravariant components (with respect to basis vectors $\boldsymbol{g}_i$) of the inverted growth tensor, and $S_{\mathrm{e},ij}$ the covariant components (with respect to basis vectors $\boldsymbol{g}^i$) of the elastic second Piola–Kirchhoff stress tensor.

The constitutive tensor with respect to the undeformed configuration is now derived by differentiating the second Piola–Kirchhoff stress tensor with respect to the Green–Lagrange strain and using Eq. (26):

$$\mathbb{D} = \frac{\partial \boldsymbol{S}}{\partial \boldsymbol{E}} \equiv 2\frac{\partial \boldsymbol{S}}{\partial \boldsymbol{C}} = 2\frac{\partial \boldsymbol{S}}{\partial \boldsymbol{C}_\mathrm{e}} : \frac{\partial \boldsymbol{C}_\mathrm{e}}{\partial \boldsymbol{C}} = 2\frac{\partial (\boldsymbol{F}_\mathrm{g}^{-1} \boldsymbol{S}_\mathrm{e} \boldsymbol{F}_\mathrm{g}^{-\top})}{\partial \boldsymbol{C}_\mathrm{e}} : \frac{\partial \boldsymbol{C}_\mathrm{e}}{\partial \boldsymbol{C}}. \tag{29}$$

Defining the elastic constitutive tensor with respect to the intermediate configuration as $\mathbb{D}_\mathrm{e} = 2\frac{\partial \boldsymbol{S}_\mathrm{e}}{\partial \boldsymbol{C}_\mathrm{e}}$, the contravariant components (with respect to $\boldsymbol{g}_i$) of the constitutive tensor are:

$$D^{ijkl} = F_\mathrm{g}^{-1,ip} F_\mathrm{g}^{-1,jq} F_\mathrm{g}^{-1,kr} F_\mathrm{g}^{-1,ls} D_{\mathrm{e},pqrs}, \tag{30}$$

with $F_\mathrm{g}^{-1,ij}$ the contravariant components (with respect to $\boldsymbol{g}_i$) of the inverted growth tensor and $D_{\mathrm{e},ijkl}$ the covariant components (with respect to $\boldsymbol{g}^i$) of the elastic constitutive tensor. For the material law in Eq. (24), the elastic constitutive tensor is

$$\begin{aligned} \mathbb{D}_\mathrm{e} =& 2\mu J_\mathrm{g} \frac{\partial J_\mathrm{e}^{-\frac{2}{3}}}{\partial \boldsymbol{C}_\mathrm{e}} \otimes \left[\boldsymbol{I} - \frac{1}{3}(\mathrm{tr}\boldsymbol{C}_\mathrm{e})\boldsymbol{C}_\mathrm{e}^{-1} \right] + 2\mu J_\mathrm{g} J_\mathrm{e}^{-\frac{2}{3}} \left[-\frac{1}{3}\frac{\partial (\mathrm{tr}\boldsymbol{C}_\mathrm{e})}{\partial \boldsymbol{C}_\mathrm{e}} \otimes \boldsymbol{C}_\mathrm{e}^{-1} - \frac{1}{3}(\mathrm{tr}\boldsymbol{C}_\mathrm{e}) \frac{\partial \boldsymbol{C}_\mathrm{e}^{-1}}{\partial \boldsymbol{C}_\mathrm{e}} \right] + \\ & 4K J_\mathrm{e} \frac{\partial J_\mathrm{e}}{\partial \boldsymbol{C}_\mathrm{e}} \otimes \boldsymbol{C}_\mathrm{e}^{-1} - 2K \frac{\partial J_\mathrm{e}}{\partial \boldsymbol{C}_\mathrm{e}} \otimes \boldsymbol{C}_\mathrm{e}^{-1} + 2K J_\mathrm{e}\,(J_\mathrm{e} - 1)\,\frac{\partial \boldsymbol{C}_\mathrm{e}^{-1}}{\partial \boldsymbol{C}_\mathrm{e}} \\ =& -\frac{2}{3}\mu J_\mathrm{g} J_\mathrm{e}^{-\frac{2}{3}} \left(\boldsymbol{C}_\mathrm{e}^{-1} \otimes \boldsymbol{I} \right) - \frac{2}{3}\mu J_\mathrm{g} J_\mathrm{e}^{-\frac{2}{3}} \left(\boldsymbol{I} \otimes \boldsymbol{C}_\mathrm{e}^{-1} \right) + \end{aligned}$$

$$\left[\frac{2}{9}\mu J_{\mathrm{g}} J_{\mathrm{e}}^{-\frac{2}{3}}(\mathrm{tr}\boldsymbol{C}_{\mathrm{e}}) + K J_{\mathrm{e}}(J_{\mathrm{e}}-1) + K J_{\mathrm{e}}^{2}\right]\left(\boldsymbol{C}_{\mathrm{e}}^{-1}\otimes\boldsymbol{C}_{\mathrm{e}}^{-1}\right) + \left[-\frac{2}{3}\mu J_{\mathrm{g}} J_{\mathrm{e}}^{-\frac{2}{3}}(\mathrm{tr}\boldsymbol{C}_{\mathrm{e}}) + 2K J_{\mathrm{e}}(J_{\mathrm{e}}-1)\right]\mathbb{I}_{\mathrm{e}}, \tag{31}$$

where the covariant components (with respect to $\boldsymbol{g}^i$) of the tensor $\mathbb{I}_{\mathrm{e}}$ in Eq. (31) are given by

$$\mathbb{I}_{\mathrm{e,ijkl}} = -\frac{1}{2}\left[C_{\mathrm{e},ik}^{-1}C_{\mathrm{e},jl}^{-1} + C_{\mathrm{e},il}^{-1}C_{\mathrm{e},jk}^{-1}\right], \tag{32}$$

and $C_{\mathrm{e},ij}^{-1}$ are the covariant components (with respect to $\boldsymbol{g}^i$) of the inverted elastic right Cauchy–Green tensor.

2.5. Variational formulation

The finite element model is derived from the principle of virtual displacements with the displacement field as the only functional unknown. As higher-order spectral interpolation functions are introduced in Section 2.6, no mixed variational methods, as used in the assumed natural strain [47] or enhanced assumed strain [48] techniques, are employed to eliminate shear or membrane locking. The functional variables in the weak formulation are therefore the displacement field $\boldsymbol{\varphi} = (\boldsymbol{v}, \boldsymbol{w}, \Psi)$ and its variation $\delta\boldsymbol{\varphi} = (\delta\boldsymbol{v}, \delta\boldsymbol{w}, \delta\Psi)$.

Due to the slow growth rates observed in most biological tissues [55], the present formulation is restricted to a quasi-static analysis with inertial terms omitted. Hence, the weak form of the equilibrium statement formulated with respect to the undeformed domain $\mathcal{B}_0$ (total Lagrangian formulation) reads

$$G(\boldsymbol{\varphi}, \delta\boldsymbol{\varphi}) = \int_{\mathcal{B}_0} \boldsymbol{S} : \delta\boldsymbol{E}\,\mathrm{d}V - \int_{\mathcal{B}_0} \delta\boldsymbol{\varphi}\cdot\boldsymbol{b}_0\,\mathrm{d}V - \int_{\partial\mathcal{B}_0} \delta\boldsymbol{\varphi}\cdot\boldsymbol{t}_0\,\mathrm{d}A = 0, \tag{33}$$

where $\boldsymbol{b}_0$ is the body force density in $\mathcal{B}_0$, and $\boldsymbol{t}_0$ is the externally prescribed traction vector acting on the boundary of the domain $\partial\mathcal{B}_0$ with unit normal vector $\boldsymbol{n}$.

As the equilibrium statement in Eq. (33) is nonlinear in $\boldsymbol{\varphi}$, it is linearised and solved using Newton's root finding algorithm. Thus,

$$G(\boldsymbol{\varphi} + \Delta\boldsymbol{\varphi}, \delta\boldsymbol{\varphi}) \approx G(\boldsymbol{\varphi}, \delta\boldsymbol{\varphi}) + DG(\boldsymbol{\varphi}, \delta\boldsymbol{\varphi})[\Delta\boldsymbol{\varphi}] = 0, \tag{34}$$

which, in combination with Eq. (33), gives

$$\int_{\mathcal{B}_0} \Delta\boldsymbol{S} : \delta\boldsymbol{E}\,\mathrm{d}V + \int_{\mathcal{B}_0} \boldsymbol{S} : \Delta(\delta\boldsymbol{E})\mathrm{d}V = -G(\boldsymbol{\varphi}, \delta\boldsymbol{\varphi}). \tag{35}$$

Due to the hyperelastic material law, *i.e.* $\mathbb{D} = \frac{\partial\boldsymbol{S}}{\partial\boldsymbol{E}}$, the second Piola–Kirchhoff stress increment $\Delta\boldsymbol{S}$ is linearly related to the Green–Lagrange strain increment $\Delta\boldsymbol{E}$, such that $\Delta\boldsymbol{S} = \mathbb{D} : \Delta\boldsymbol{E}$. In indicial notation, the linearised equilibrium equation (35) therefore reads

$$\begin{aligned} &\int_{\mathcal{B}_0} \Delta S^{ij}\delta E_{ij} J\mathrm{d}\xi^1\mathrm{d}\xi^2\mathrm{d}\xi^3 + \int_{\mathcal{B}_0} S^{ij}\Delta(\delta E)_{ij} J\mathrm{d}\xi^1\mathrm{d}\xi^2\mathrm{d}\xi^3 = -G \\ \therefore &\int_{\mathcal{B}_0} D^{ijkl}\Delta E_{kl}\delta E_{ij} J\mathrm{d}\xi^1\mathrm{d}\xi^2\mathrm{d}\xi^3 + \int_{\mathcal{B}_0} S^{ij}\Delta(\delta E)_{ij} J\mathrm{d}\xi^1\mathrm{d}\xi^2\mathrm{d}\xi^3 = -G, \end{aligned} \tag{36}$$

with all quantities conveniently evaluated with respect to the covariant ($\boldsymbol{g}_i$) and contravariant ($\boldsymbol{g}^i$) basis vectors associated with the shell geometry. The indicial components $\delta E_{ij} = \delta\epsilon_{ij} + \xi^3\delta\kappa_{ij}$ and $\Delta(\delta E)_{ij} = \Delta(\delta\epsilon)_{ij} + \xi^3\Delta(\delta\kappa)_{ij}$ are expanded in Appendix A based on the expressions for ϵ_{ij} and κ_{ij} in Eq. (19).

2.6. Higher-order spectral interpolation functions

For this morphoelastic shell element we define a set of quadrilateral elements based on higher-order polynomial basis functions. The accuracy of the model can therefore be improved through h-refinement (smaller element sizes), p-refinement (increasing the polynomial order and nodes per element), or hp-refinement (a combination of both). An advantage of high p-refinement is that it overcomes the poor performance of low-order morphoelastic finite elements [23,51]. Furthermore, shear and membrane locking are practically non-existent even for full integration of all quantities in the direct displacement-based formulation.

The two-dimensional basis functions $\psi_k(\xi^1, \xi^2)$ in the natural coordinates (ξ^1, ξ^2) of the master element $\hat{\Omega}^e$ are constructed from the product of the one-dimensional spectral nodal interpolation functions [49]

$$\zeta_i(\xi) = \frac{(\xi - 1)(\xi + 1)L_{p,\xi}(\xi)}{p(p+1)L_p(\xi_i)(\xi - \xi_i)}, \tag{37}$$

where $L_p(\xi)$ is the Legendre polynomial of order p and $L_{p,\xi} = \frac{\mathrm{d}L_p}{\mathrm{d}\xi}$. The coordinates ξ_i refer to the nodes of the 1D interpolants and are located by solving for the roots of

$$(\xi - 1)(\xi + 1)L_{p,\xi}(\xi) = 0 \quad \text{for} \quad \xi \in [-1, 1]. \tag{38}$$

Hence, the nodal coordinates lie on a Chebychev–Gauss–Lobatto grid with nodal position bias towards the edges of the domain. These spectral one-dimensional interpolation functions are then extended onto the bi-unit master square by multiplication of two interpolation functions, *i.e.* $\zeta_i(\xi^1)$ and $\zeta_j(\xi^2)$

$$\psi_k(\xi^1, \xi^2) = \zeta_i(\xi^1)\zeta_j(\xi^2) \quad \text{for} \quad (\xi^1, \xi^2) \in [-1, 1]^2, \tag{39}$$

where $k = i + (j-1)(p+1)$ and $i, j = 1, \ldots, p+1$. Each quadrilateral finite element thus has $(p+1)^2$ nodes and the order of the element can be refined by increasing the value of p. In the present work, 25-noded elements with $p = 4$ are used as they represent a good trade-off between the benefits of higher-order interpolation and the computational efficiency of lower matrix bandwidth.

3. Morphoelastic instability analysis using generalised path-following

This section discusses a morphoelastic computational stability framework based on generalised path-following [56]. In particular, nonlinear instability analysis based on extended systems for direct pinpointing of critical points and branch switching facilitates a comprehensive exploration of growth-mediated morphogenesis. The general setting is presented in Section 3.1 with an application to morphoelastic equilibrium curves in Section 3.2. Pinpointing of critical points while path-following morphoelastic equilibrium curves is discussed in Section 3.3 and branch switching onto bifurcated paths at branching points is discussed in Section 3.5. For further details on the concept of generalised path-following, the interested reader is directed to Eriksson [56] and Groh et al. [57].

3.1. General setting

When discretised using a finite element interpolation, the weak form of the equilibrium equation (36) is expressed as a balance between internal nodal forces $\boldsymbol{f}$, and externally applied nodal forces $\boldsymbol{p}$,

$$\boldsymbol{R}(\boldsymbol{u}, \boldsymbol{\Lambda}) = \boldsymbol{f}(\boldsymbol{u}, \boldsymbol{\Lambda}_\mathrm{i}) - \boldsymbol{p}(\boldsymbol{\Lambda}_\mathrm{e}) = \boldsymbol{0}. \tag{40}$$

Here, the vector $\boldsymbol{u}$ represents n displacement degrees-of-freedom (dofs) and the vector $\boldsymbol{\Lambda} = [\boldsymbol{\Lambda}_\mathrm{i}^\top, \boldsymbol{\Lambda}_\mathrm{e}^\top]^\top = [\lambda_1, \ldots, \lambda_p]^\top$ contains p control parameters with $\boldsymbol{\Lambda}_\mathrm{i}$ representing internal parameters (*e.g.* growth parameter, material properties, geometric dimensions, temperature fields) and $\boldsymbol{\Lambda}_\mathrm{e}$ external loading parameters (*e.g.* forces, moments, tractions). For morphoelastic problems we isolate the growth parameter $\lambda_\mathrm{g} \in \boldsymbol{\Lambda}_\mathrm{i}$ that is used to parametrise the growth tensor, $\boldsymbol{F}_\mathrm{g} = \boldsymbol{F}_\mathrm{g}(\lambda_\mathrm{g})$. The external (non-follower) loading vector $\boldsymbol{p}$ is defined by $\boldsymbol{p}(\boldsymbol{\Lambda}_\mathrm{e}) = \hat{\boldsymbol{P}}\boldsymbol{\Lambda}_\mathrm{e}$, where $\hat{\boldsymbol{P}}$ is a matrix with each column an externally applied load vector $\hat{\boldsymbol{p}}_i$ scaled through the associated i^{th} component of $\boldsymbol{\Lambda}_\mathrm{e}$, $\lambda_e^i \in \boldsymbol{\Lambda}_\mathrm{e}$.

As the n number of equilibrium equations $\boldsymbol{R}$ of Eq. (40) are functions of n displacement dofs and p system parameters, a p-dimensional solution manifold exists in $\mathbb{R}^{(n+p)}$. By extending the equilibrium equations $\boldsymbol{R}$ through $r \leq p-1$ constraining equations $\boldsymbol{g}$, specific solution subsets on the p-dimensional solution manifold are defined

$$\boldsymbol{G}(\boldsymbol{u}, \boldsymbol{\Lambda}) \equiv \begin{pmatrix} \boldsymbol{R}(\boldsymbol{u}, \boldsymbol{\Lambda}) \\ \boldsymbol{g}(\boldsymbol{u}, \boldsymbol{\Lambda}) \end{pmatrix} = \boldsymbol{0}. \tag{41}$$

When r auxiliary equations are defined, the solution to Eq. (41) is $(p-r)$-dimensional. Hence, $r = p-1$ auxiliary equations are required to define a one-dimensional solution curve in $\mathbb{R}^{(n+p)}$.

In this manner different equilibrium paths can be determined by varying any parameter in the set $\boldsymbol{\Lambda}$. This means the computationally expensive parametric approach of running multiple equilibrium curves with varying growth parameter λ_g, each with different geometric and/or material properties, is precluded. Instead, an equilibrium curve

$\boldsymbol{u} = \boldsymbol{u}(\lambda_g)$ for a single baseline model can be determined, and specific points of interest then traced through parameter space. This treatment naturally leads to the notion of tracing critical points. As the onset of instability or the exchange of stability are often linked directly to pattern formation in morphoelastic problems, *e.g.* through wrinkling, the ability to trace critical curves directly through parameter space is invaluable for quickly ascertaining the sensitivity of different pattern formation phenomena to changing model parameters.

For example, to constrain the system of n equilibrium equations $\boldsymbol{R}$ to a locus of critical points, we enforce a singularity condition such as $\boldsymbol{K}_T\boldsymbol{\phi} = \boldsymbol{0}$, *i.e.* at least one eigenvector $\boldsymbol{\phi}$ of the tangential stiffness matrix $\boldsymbol{K}_T = \boldsymbol{R}_{,\boldsymbol{u}} = \boldsymbol{f}_{,\boldsymbol{u}}$ spans the nullspace. In the most general form, not limited to but including the previous singularity condition, a vector of q auxiliary variables $\boldsymbol{v}$ is added to the auxiliary equations $\boldsymbol{g}$,

$$\boldsymbol{G}(\boldsymbol{u}, \boldsymbol{\Lambda}, \boldsymbol{v}) \equiv \begin{pmatrix} \boldsymbol{R}(\boldsymbol{u}, \boldsymbol{\Lambda}) \\ \boldsymbol{g}(\boldsymbol{u}, \boldsymbol{\Lambda}, \boldsymbol{v}) \end{pmatrix} = \boldsymbol{0}. \tag{42}$$

Eq. (42) defines $n + r$ equations in $(n + p + q)$ unknowns leading to a $(p + q - r)$-dimensional solution manifold.

The system of equations for a one-dimensional equilibrium curve defined by a single parameter, *i.e.* $\boldsymbol{u} = \boldsymbol{u}(\lambda)$ for $\lambda \in \boldsymbol{\Lambda}$, is recovered by setting $p = 1$ and $q = r = 0$. Alternatively, a one-dimensional curve of critical points defined by two simultaneously varying parameters $p = 2$, *e.g.* a growth parameter and a material/geometric property, would define the n-dimensional null vector at the critical state as an auxiliary variable, *i.e.* $\boldsymbol{v} = \boldsymbol{\phi}$ with $q = n$, and the criticality condition with an additional norming constraint as the auxiliary equations, *i.e.* $\boldsymbol{g} = \{\boldsymbol{K}_T\boldsymbol{v}; \quad \|\boldsymbol{v}\|_2 - 1\}$ with $r = n + 1$.

3.2. Path-following morphoelastic equilibrium curves

An important assumption in evaluating morphoelastic equilibrium curves is that growth and atrophy are reversible processes. This is an important difference to the case of plasticity where plastic deformations cannot be undone and are accumulated throughout a loading history. Hence, we assume that the scalar growth parameter λ_g can both increase and decrease throughout a morphoelastic evolution to represent addition/growth and subtraction/atrophy of mass, respectively. An interchange between these two phenomena can occur at a maximum or minimum turning/limit point on the morphoelastic equilibrium curve, and under monotonically increasing or decreasing growth factor, the biomaterial would dynamically snap to an alternative morphology at such a point. It is useful to trace out the full morphoelastic equilibrium curve comprised of statically stable and unstable segments—even if growth monotonically increases throughout a biological process—as this allows alternative morphologies to be computationally determined by exploring the entire equilibrium manifold. As shown in Section 4, different stable morphologies can exist for the same system and level of growth, *i.e.* the morphoelastic equilibrium manifold shows areas of multi-stability.

Returning to the system of Eqs. (42), when evaluating one-dimensional curves, *i.e.* $r = p + q - 1$, one additional constraining equation is needed to uniquely solve for a solution point $\boldsymbol{y} = (\boldsymbol{u}, \boldsymbol{\Lambda}, \boldsymbol{v})$. Hence,

$$\boldsymbol{G}^\sigma(\boldsymbol{y}) \equiv \begin{pmatrix} \boldsymbol{R}(\boldsymbol{u}, \boldsymbol{\Lambda}) \\ \boldsymbol{g}(\boldsymbol{u}, \boldsymbol{\Lambda}, \boldsymbol{v}) \\ \sigma(\boldsymbol{u}, \boldsymbol{\Lambda}) \end{pmatrix} = \boldsymbol{0}, \tag{43}$$

where σ is a scalar equation that plays the role of a multi-dimensional arc-length constraint along a specific direction of the one-dimensional curve. A solution to Eq. (43) is determined by a consistent linearisation coupled with Newton's root-finding algorithm,

$$\boldsymbol{y}_k^{j+1} = \boldsymbol{y}_k^j - \left\{\boldsymbol{G}^\sigma_{,\boldsymbol{y}}(\boldsymbol{y}_k^j)\right\}^{-1} \cdot \boldsymbol{G}^\sigma(\boldsymbol{y}_k^j) = \boldsymbol{y}_k^j + \delta\boldsymbol{y}_k^j, \tag{44}$$

where the superscript denotes the jth equilibrium iteration and the subscript the kth solution increment. For most problems, the inversion of the iteration matrix

$$\boldsymbol{G}^\sigma_{,\boldsymbol{y}} = \begin{bmatrix} \boldsymbol{K}_T & \boldsymbol{R}_{,\boldsymbol{\Lambda}} & \boldsymbol{0}_{n\times q} \\ \boldsymbol{g}_{,\boldsymbol{u}} & \boldsymbol{g}_{,\boldsymbol{\Lambda}} & \boldsymbol{g}_{,\boldsymbol{v}} \\ \sigma^\top_{,\boldsymbol{u}} & \sigma^\top_{,\boldsymbol{\Lambda}} & \boldsymbol{0}_{1\times q} \end{bmatrix}, \tag{45}$$

is significantly simplified by partitioning the system into blocks such that only the symmetric tangential stiffness matrix $\boldsymbol{K}_T = \boldsymbol{R}_{,\boldsymbol{u}} = \boldsymbol{f}_{,\boldsymbol{u}}$ needs to be factorised in the solution process (see, *e.g.*, [53] for details).

For path following a morphoelastic equilibrium curve $\boldsymbol{u} = \boldsymbol{u}(\lambda_\mathrm{g})$, the equations are restricted to one varying parameter $\lambda_\mathrm{g} \in \boldsymbol{\Lambda}_\mathrm{i}$ with all other parameters $\boldsymbol{\Lambda}^\mathrm{c} = (\boldsymbol{\Lambda}^\mathrm{c}_\mathrm{i}, \boldsymbol{\Lambda}^\mathrm{c}_\mathrm{e}) \subset \boldsymbol{\Lambda}$, $\lambda_\mathrm{g} \notin \boldsymbol{\Lambda}^\mathrm{c}$ held constant. We therefore have the equilibrium equations

$$\boldsymbol{R}(\boldsymbol{u}, \lambda_\mathrm{g}, \boldsymbol{\Lambda}^\mathrm{c}) = \boldsymbol{f}(\boldsymbol{u}, \lambda_\mathrm{g}, \boldsymbol{\Lambda}^\mathrm{c}_\mathrm{i}) - \hat{\boldsymbol{P}}\boldsymbol{\Lambda}^\mathrm{c}_\mathrm{e} = \boldsymbol{0} \tag{46}$$

constrained by: (i) the auxiliary equations $\boldsymbol{g} = \boldsymbol{\Lambda}^c - \boldsymbol{\Sigma} = \boldsymbol{0}$, which prescribe the values $\boldsymbol{\Sigma}$ to all non-varying parameters $\boldsymbol{\Lambda}^\mathrm{c}$, and (ii) the arc-length constraint $\sigma(\boldsymbol{u}, \lambda_\mathrm{g}) = \boldsymbol{n}_u^\top \boldsymbol{u} + n_{\lambda_\mathrm{g}}\lambda_\mathrm{g} - \sigma_\mathrm{c} = 0$, to give

$$\boldsymbol{G}^\sigma(\boldsymbol{u}, \lambda_\mathrm{g}, \boldsymbol{\Lambda}^\mathrm{c}) \equiv \begin{pmatrix} \boldsymbol{R}(\boldsymbol{u}, \lambda_\mathrm{g}, \boldsymbol{\Lambda}^\mathrm{c}) \\ \boldsymbol{\Lambda}^\mathrm{c} - \boldsymbol{\Sigma} \\ \sigma(\boldsymbol{u}, \lambda_\mathrm{g}) \end{pmatrix} = \boldsymbol{0}. \tag{47}$$

Linearisation of the above equation leads to

$$\begin{bmatrix} \boldsymbol{K}_\mathrm{T} & \boldsymbol{R}_{,\lambda_\mathrm{g}} & \boldsymbol{R}_{,\boldsymbol{\Lambda}^\mathrm{c}} \\ \boldsymbol{0}_{(p-1)\times n} & \boldsymbol{0}_{(p-1)\times 1} & \boldsymbol{1}_{(p-1)\times(p-1)} \\ \boldsymbol{n}_u^\top & n_{\lambda_\mathrm{g}} & \boldsymbol{0}_{1\times(p-1)} \end{bmatrix} \begin{Bmatrix} \delta\boldsymbol{u} \\ \delta\lambda_\mathrm{g} \\ \delta\boldsymbol{\Lambda}^\mathrm{c} \end{Bmatrix} = - \begin{Bmatrix} \boldsymbol{R}(\boldsymbol{u}, \lambda_\mathrm{g}, \boldsymbol{\Lambda}^\mathrm{c}) \\ \boldsymbol{\Lambda}_\mathrm{c} - \boldsymbol{\Sigma} \\ \sigma(\boldsymbol{u}, \lambda_\mathrm{g}) \end{Bmatrix}, \tag{48}$$

where $\boldsymbol{1}$ is the identity matrix. The 2nd row and 3rd column of the iteration matrix can generally be omitted as $\delta\boldsymbol{\Lambda}^\mathrm{c} = \boldsymbol{0}$ by definition. The term $\boldsymbol{R}_{,\lambda_\mathrm{g}}$ is computed via a forward finite difference scheme

$$\boldsymbol{R}_{,\lambda_\mathrm{g}} = \boldsymbol{f}_{,\lambda_\mathrm{g}} \approx \frac{\boldsymbol{f}(\boldsymbol{u}, \lambda_\mathrm{g} + \varepsilon|\lambda_\mathrm{g}|, \boldsymbol{\Lambda}^\mathrm{c}_\mathrm{i}) - \boldsymbol{f}(\boldsymbol{u}, \lambda_\mathrm{g}, \boldsymbol{\Lambda}^\mathrm{c}_\mathrm{i})}{\varepsilon|\lambda_\mathrm{g}|}, \tag{49}$$

where ε is a small perturbation parameter in the range of 10^{-5}–10^{-8}. $\boldsymbol{R}_{,\lambda_\mathrm{g}}$ represents the "forcing" vector that leads to a change in the displacement field $\boldsymbol{u}$ as the growth parameter λ_g is changed. Put differently, as λ_g is incremented away from a known equilibrium solution, the vector $\boldsymbol{K}_\mathrm{T}^{-1}\boldsymbol{R}_{,\lambda_\mathrm{g}}$ corresponds to the tangential change in the displacement field.

3.3. Pinpointing critical points

Pinpointing critical points allows the exact value of morphoelastic instability points, *i.e.* points where the deformation mode of the growing body changes qualitatively, to be determined. Furthermore, if the critical point is of the bifurcation/branching type, then branch switching can uncover new morphological evolution trajectories that branch-off the critical point.

To pinpoint critical points, an augmented system of the form described by Eq. (42) is formulated. The advantage of this method is that the singularity condition forces Newton's method to converge to the critical point directly in a single solution increment. Here, the nullvector approach described by Moore and Spence [58] and applied to the finite element method by Wriggers and Simo [53] is used. The nullvector method is based on the fact that the tangential stiffness matrix $\boldsymbol{K}_\mathrm{T}$ has at least one zero eigenvalue $\mu = \boldsymbol{\phi}^\top \boldsymbol{K}_\mathrm{T}\boldsymbol{\phi}$ at a critical point. Therefore, the associated eigenvector $\boldsymbol{\phi}$ is in the nullspace of $\boldsymbol{K}_\mathrm{T}$. For the morphoelastic system we have

$$\boldsymbol{G}(\boldsymbol{u}, \lambda_\mathrm{g}, \boldsymbol{\Lambda}^\mathrm{c}, \boldsymbol{\phi}) \equiv \begin{pmatrix} \boldsymbol{R}(\boldsymbol{u}, \lambda_\mathrm{g}, \boldsymbol{\Lambda}^\mathrm{c}) \\ \boldsymbol{K}_\mathrm{T}(\boldsymbol{u}, \lambda_\mathrm{g}, \boldsymbol{\Lambda}^\mathrm{c}_\mathrm{i})\boldsymbol{\phi} \\ \|\boldsymbol{\phi}\|_2 - 1 \end{pmatrix} = \boldsymbol{0}, \tag{50}$$

where the norm of the nullvector is required to eliminate the trivial solution $\boldsymbol{\phi} = \boldsymbol{0}$. Eq. (50) features $(2n + 1)$ equations in $(2n + p)$ variables, and the $(p - 1)$ extra equations required to solve the system are implicit in the definition that the added control parameters in $\boldsymbol{\Lambda}^\mathrm{c}$ are held constant, *i.e.* $\Lambda^{\mathrm{c}j} = \Sigma_j$ for $j = 2 \ldots p$ (see Eq. (48)). The resulting system of equations can therefore be solved via Newton's root-finding algorithm for the critical point $(\boldsymbol{u}^*, \lambda^*_\mathrm{g}, \boldsymbol{\Lambda}^\mathrm{c})$ as well as the associated nullvector $\boldsymbol{\phi}$. The solution process follows the typical predictor–corrector scheme with the iteration matrix derived from the linearisation of Eq. (50),

$$\begin{bmatrix} \boldsymbol{K}_\mathrm{T} & \boldsymbol{R}_{,\lambda_\mathrm{g}} & \boldsymbol{0} \\ (\boldsymbol{K}_\mathrm{T}\boldsymbol{\phi})_{,\boldsymbol{u}} & (\boldsymbol{K}_\mathrm{T}\boldsymbol{\phi})_{,\lambda_\mathrm{g}} & \boldsymbol{K}_\mathrm{T} \\ \boldsymbol{0}_{1\times n} & 0 & \frac{\boldsymbol{\phi}^\top}{\|\boldsymbol{\phi}\|_2} \end{bmatrix} \begin{Bmatrix} \delta\boldsymbol{u} \\ \delta\lambda_\mathrm{g} \\ \delta\boldsymbol{\phi} \end{Bmatrix} = - \begin{Bmatrix} \boldsymbol{R}(\boldsymbol{u}, \lambda_\mathrm{g}, \boldsymbol{\Lambda}^\mathrm{c}) \\ \boldsymbol{K}_\mathrm{T}(\boldsymbol{u}, \lambda_\mathrm{g}, \boldsymbol{\Lambda}^\mathrm{c}_\mathrm{i})\boldsymbol{\phi} \\ \|\boldsymbol{\phi}\|_2 - 1 \end{Bmatrix}. \tag{51}$$

Following Wriggers and Simo [53], approximate directional derivatives of the tangential stiffness matrix can be computed by

$$(\boldsymbol{K}_{\mathrm{T}}\boldsymbol{\phi})_{,\boldsymbol{u}} \approx \frac{\boldsymbol{K}_{\mathrm{T}}(\boldsymbol{u}+\varepsilon\|\boldsymbol{u}\|_2\boldsymbol{\phi},\,\lambda_{\mathrm{g}},\,\boldsymbol{\Lambda}_{\mathrm{i}}^{\mathrm{c}}) - \boldsymbol{K}_{\mathrm{T}}(\boldsymbol{u},\,\lambda_{\mathrm{g}},\,\boldsymbol{\Lambda}_{\mathrm{i}}^{\mathrm{c}})}{\varepsilon\|\boldsymbol{u}\|_2}, \tag{52a}$$

$$(\boldsymbol{K}_{\mathrm{T}}\boldsymbol{\phi})_{,\lambda_{\mathrm{g}}} \approx \frac{\boldsymbol{K}_{\mathrm{T}}(\boldsymbol{u},\,\lambda_{\mathrm{g}}+\varepsilon|\lambda_{\mathrm{g}}|,\,\boldsymbol{\Lambda}_{\mathrm{i}}^{\mathrm{c}}) - \boldsymbol{K}_{\mathrm{T}}(\boldsymbol{u},\,\lambda_{\mathrm{g}},\,\boldsymbol{\Lambda}_{\mathrm{i}}^{\mathrm{c}})}{\varepsilon|\lambda_{\mathrm{g}}|}\boldsymbol{\phi}, \tag{52b}$$

with ε in the range of 10^{-5}–10^{-8}. Once a critical point has been pinpointed, we distinguish the type of critical point on the equilibrium curve using the following criteria:

- if $\boldsymbol{\phi}\cdot\boldsymbol{R}_{,\lambda_{\mathrm{g}}} = 0$, the critical point is a bifurcation/branching point;
- if $\boldsymbol{\phi}\cdot\boldsymbol{R}_{,\lambda_{\mathrm{g}}} \neq 0$, the critical point is a limit/turning point.

If a bifurcation/branching point has been determined, branch switching onto a bifurcated path can be initiated by inserting the critical eigenvector $\boldsymbol{\phi}$ into the predictor of the next loading increment (see Section 3.5). When solving the system of Eqs. (51), the iteration matrix is not inverted in its entirety, but split into individual blocks and Eq. (51) solved by a partitioning procedure in such a manner that only the symmetric tangential stiffness matrix is factorised (see Wriggers and Simo [53]).

The implemented pinpointing procedure proceeds as follows. While path-following along a morphoelastic equilibrium path, the pivots of the tangent stiffness matrix are monitored efficiently using an **LDL**-decomposition ($\boldsymbol{K}_{\mathrm{T}}$ is Hermitian). When the number of negative pivots in the **D**-matrix between two consecutive converged equilibrium solutions changes, a critical point must exist between the two solution points and the pinpointing procedure is started. The eigenvector $\boldsymbol{\phi}_{\mathrm{s}}$ associated with the smallest-magnitude eigenvalue at the last converged equilibrium state ($\boldsymbol{u}^1$, λ_{g}^1, $\boldsymbol{\Lambda}^{\mathrm{c}}$) is then extracted (*e.g* using the EIGS function in MATLAB) and seeded alongside ($\boldsymbol{u}^1$, λ_{g}^1, $\boldsymbol{\Lambda}^{\mathrm{c}}$) as the starting point for the iterative critical point pinpointing procedure. If the solver does not converge, then an additional equilibrium point between the two previously determined equilibria is determined and the process is repeated.

3.4. Multi-parametric loci of critical points

If Eq. (50) is extended by an arc-length equation and one additional system parameter λ_{a}, initially in the set of constant parameters $\boldsymbol{\Lambda}^{\mathrm{c}}$, is also allowed to vary, then we can trace the locus of a critical point through parameter space. Hence, we path-follow along a critical cutset of the equilibrium manifold with two varying parameters $\boldsymbol{u}^* = \boldsymbol{u}(\lambda_{\mathrm{g}}^*, \lambda_{\mathrm{a}})$, with the critical growth parameter a function of the second parameter $\lambda_{\mathrm{g}}^* = \lambda_{\mathrm{g}}^*(\lambda_{\mathrm{a}})$. Owing to the singularity of the tangent stiffness matrix $\boldsymbol{K}_{\mathrm{T}}$, tracking the locus of critical points requires careful consideration of the tangent space at each critical point. These considerations are outlined in detail, for example, in Eriksson [56] and Groh et al. [57]. In Section 5, the ability to track critical points through parameter space is used to quantify the effect of material parameters on critical growth factors.

3.5. Branch switching at bifurcation/branching points

In the case of a simple degeneracy of the tangential stiffness matrix, the simplest method of branch switching between two intersecting equilibrium paths is to insert the critical eigenvector into the displacement field at the bifurcation point [59]. The critical eigenvector $\boldsymbol{\phi}$ at the bifurcation point is thus used as a perturbation to the known critical solution $\boldsymbol{u}^*$:

$$\boldsymbol{u}^{\mathrm{p}} = \boldsymbol{u}^* + \iota\frac{\boldsymbol{\phi}}{\|\boldsymbol{\phi}\|_2}, \tag{53}$$

with the perturbed configuration $\boldsymbol{u}^{\mathrm{p}}$ acting as a predictor for the first step on a new path starting from the bifurcation point. The magnitude of the scaling factor ι is determined from

$$\iota = \pm\frac{\|\boldsymbol{u}^*\|_2}{\tau}, \tag{54}$$

where the sign of ι controls the direction of path-following along the bifurcated path, and τ is a problem-specific constant in the range of 10^{-3}–10^{3}. If τ is too small, then the algorithm may continue on the known primary path, and if τ is too large, then the solver may not converge.

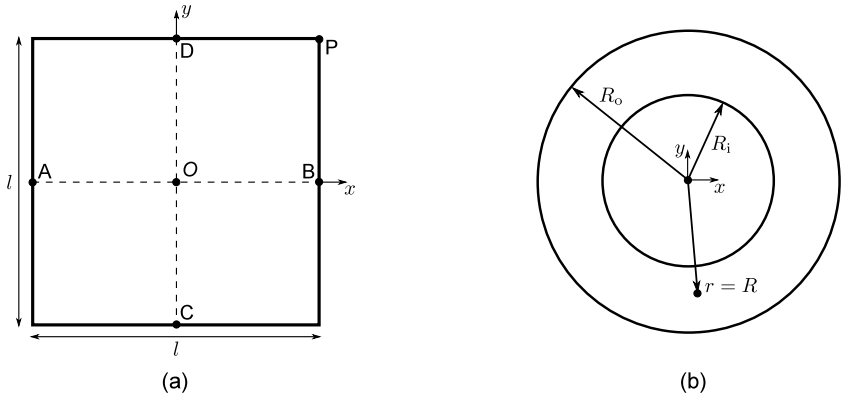

Fig. 3. Geometry used for (a) free growth of a flat plate and (b) constrained growth of an annulus.

4. Numerical applications to planar growth

The seven-parameter morphoelastic shell element is applied to a number of planar growth problems, and the ensuing quasi-static nonlinear equations are solved using the computational stability framework introduced in Section 3. In each example, the growth tensor is defined as a model input and takes the form

$$\boldsymbol{F}_{\mathrm{g}}(\boldsymbol{X}, \lambda_{\mathrm{g}}) = \begin{bmatrix} g_1(\boldsymbol{X}, \lambda_{\mathrm{g}}) & 0 & 0 \\ 0 & g_2(\boldsymbol{X}, \lambda_{\mathrm{g}}) & 0 \\ 0 & 0 & 1 \end{bmatrix}. \tag{55}$$

The growth tensor is specified at the Gauss integration points of each shell element, and the components of $\boldsymbol{F}_{\mathrm{g}}$ are defined in a local Cartesian coordinate system $\{\boldsymbol{e}_1, \boldsymbol{e}_2, \boldsymbol{e}_3\}$ lying in the plane of the shell at each Gauss point.[3] such that there is no growth in the thickness $\boldsymbol{e}_3$ direction. Note, due to the total Lagrangian formulation, the functional dependence of $\boldsymbol{F}_{\mathrm{g}}$ is always with respect to the undeformed material coordinates $\boldsymbol{X}$ and a coordinate system defined in the original, undeformed configuration.

We restrict ourselves to stress- and strain-independent definitions of the two growth functions $g_\alpha(\boldsymbol{X}, \lambda_{\mathrm{g}})$, noting that stress- or strain-dependent growth could readily be incorporated in the computer implementation. The focus herein is particularly on spatially varying growth with the ensuing differential growth conducive to instability phenomena and pattern formation. Following commonly observed spatial distributions of growth laws in biological tissues (*e.g.* leaves [3] and petals [6]), exponential and/or power law distributions of growth towards edges are predominantly assumed.

In Section 4.1 the seven-parameter element is first validated against the solid-shell element of Zheng et al. [37] for a freely growing flat plate and a constrained growing annulus. The importance of monitoring the stability of the computed equilibria is especially highlighted as this was not considered by Zheng et al. [37]. Section 4.2 introduces the general capabilities of the morphoelastic stability framework using the example of a growing annulus. In Section 4.3 the stability framework is used to highlight the governing role of exponential edge growth in driving fractal rippling patterns in a long sheet. Sections 4.4–4.6 then demonstrate the mechanics of this pattern formation in various biological examples, such as in the fronds of hart's-tongue fern (Section 4.4), daffodil coronas (Section 4.5), and the blooming of lily petals (Section 4.6).

4.1. Model validation: a growing plate and annulus

Free growth of a square plate and constrained growth of an annulus are first considered to validate the morphoelastic seven-parameter model against a solid-shell element in the literature [37]. The geometries of these two problems are schematically shown in Fig. 3.

[3] In the computer implementation, the defined local Cartesian components of $\boldsymbol{F}_{\mathrm{g}}$ are transposed into covariant and contravariant components corresponding to the convected bases $\boldsymbol{g}^i$ and $\boldsymbol{g}_i$ to facilitate their implementation as outlined in Section 2.4.

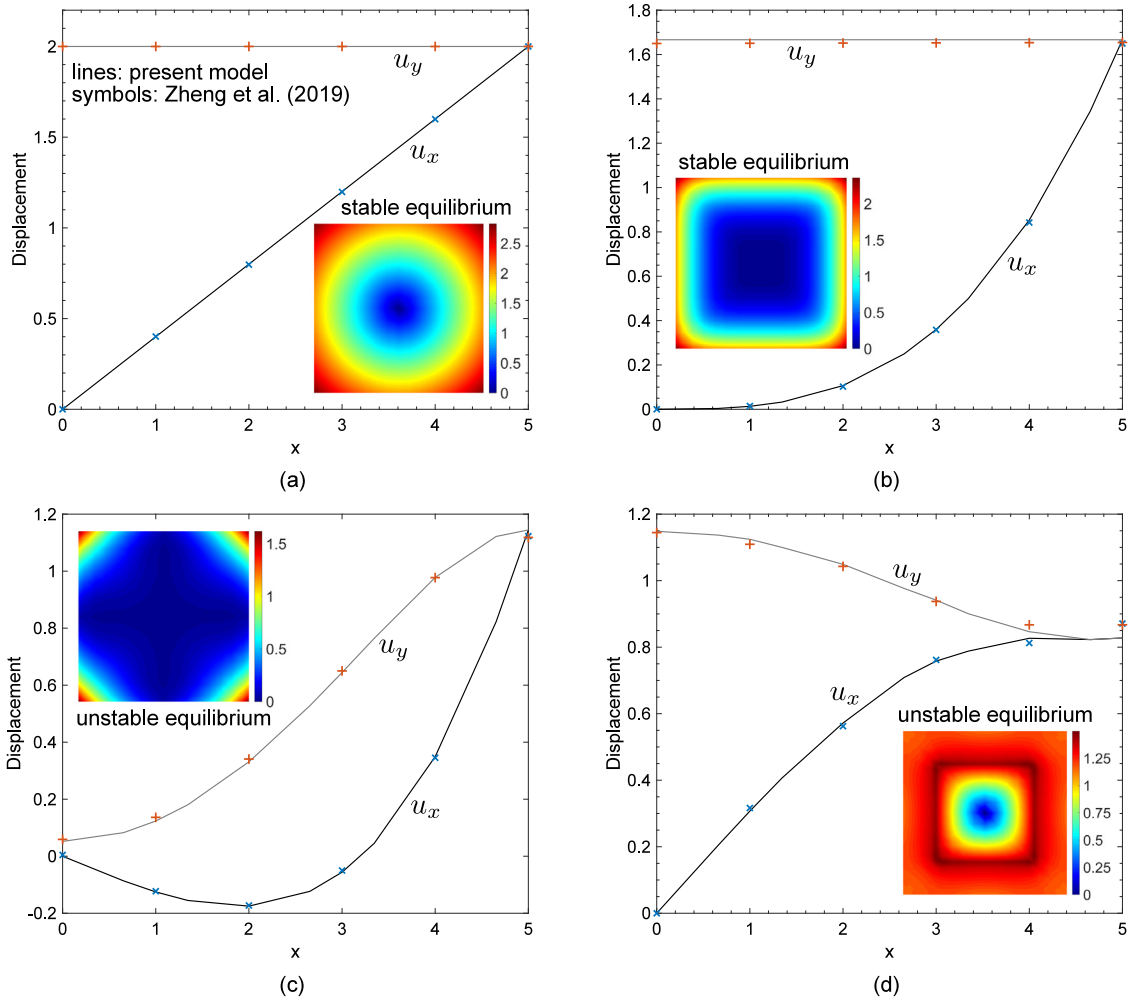

Fig. 4. Variation of x- and y-displacement along edge DP of the flat plate (see Fig. 3a) with the four growth laws (i)–(iv) described in the text. The present model matches the results by Zheng et al. [37]. The inset contours show the final (flat) deformation mode after growth. In figures (c) and (d) these fundamental flat states are statically unstable and would not be observed in reality.

Following Zheng et al. [37], the flat plate has a square geometry with a side length of $l = 10$ and a thickness of $h = 0.01$. The plate is discretised using a regular mesh of 21×21 nodes that are arranged into 25 higher-order shell elements (25 nodes per element). The centroid O of the plate is constrained in all three Cartesian directions; the line AB is constrained from moving in the y-direction and the shell normals on line AB cannot rotate around the x-axis; the line CD is constrained from moving in the x-direction and shell normals on line CD cannot rotate around the y-axis; and all four points A, B, C, and D are constrained from moving in the out-of-plane z-direction. The shear modulus of the plate is taken as $\mu = 4\times10^3$ and the bulk modulus as $K = 4\times10^5$ to give an effective Poisson's ratio of $\nu = 0.495$. The plate grows to a final growth deformation tensor of $\boldsymbol{F}_{\mathrm{g}} = \mathrm{diag}(g_x, g_y, 1)$, where the components refer to the xyz-coordinate system in Fig. 3a, with four different scenarios considered: (i) $g_x = g_y = 1.4$; (ii) $g_x = 1 + (x/5)^2$ and $g_y = 1 + (y/5)^2$; (iii) $g_x = g_y = 1 + (x/5)^2(y/5)^2$; and (iv) $g_x = g_y = 1.5$ for $-3 \le x \le 3$, $-3 \le y \le 3$ and $g_x = g_y = 1$ elsewhere. For all position-dependent growth laws, the coordinates (x, y) refer to the original, undeformed locations of all material points. For every model, the nonlinear solver converged to the target growth state within a single load increment.

Fig. 4a–d show the variation of the x- and y-displacements (u_x and u_y) along line DP for cases (i)–(iv), respectively, with contour plots of the corresponding displacement magnitudes shown as insets. In all four cases, the seven-parameter shell element matches the results by Zheng et al. [37] with small differences attributable to the finer

mesh used in the present paper (11×11 nodes per plate quarter compared to 6×6 nodes per plate quarter in [37]). The uniform and spatially varying growth laws in cases (i) and (ii), respectively, correspond to compatible growth fields, such that the ensuing deformations are stress free, and as noted in Fig. 4a–b, the corresponding equilibrium states are statically stable. The displacement variations and deformation contour plots for cases (iii) and (iv) are more complicated due to the non-compatible growth fields that lead to self-restraining deformations. Indeed, the deformed equilibria for cases (iii) and (iv) are highly unstable, as noted in Fig. 4c–d, with a total of 133 and 135 negative eigenvalues in the tangent stiffness matrix, respectively. The applied growth fields (iii) and (iv) thus lead to bifurcations away from the fundamental flat state well before reaching the growth values specified, thereby highlighting the importance of tracking stability properties throughout morphoelastic analyses of thin biological materials. Indeed, if a dynamic or experimental instantiation of growth cases (iii) and (iv) were to be considered, the flat deformation fields corresponding to the contours in Fig. 4c–d would not be realised.

The importance of stability tracking throughout a nonlinear morphoelastic solution procedure is highlighted further with the second verification model proposed by Zheng et al. [37]. A thin annulus with inside radius $R_\mathrm{i} = 1$ and outside radius $R_\mathrm{o} = 2$ (see Fig. 3b) of thickness $h = 0.001$ is discretised using 17 radial and 80 circumferential nodes that are assembled into a uniform mesh of 80 25-noded shell elements. The shear modulus is again taken to be $\mu = 4 \times 10^3$ and the bulk modulus $K = 4 \times 10^5$. The planar growth law is $\boldsymbol{F}_\mathrm{g} = \mathrm{diag}(g_r, g_\theta, 1)$ where the subscripts (r, θ) refer to the radial and azimuthal coordinates of a cylindrical coordinate system, respectively. Two different growth laws are assumed: (1) $g_r = g_\theta = 1.35$; and (2) $g_r = g_\theta = (r - 1.5)^2 + 1.1$, where r is the radial position of material points in the undeformed configuration. In addition, either (A) the inside radius $r = R_\mathrm{i} = 1$; or (B) the outside radius $r = R_\mathrm{o} = 2$ is restrained from displacing in all three Cartesian directions, giving a total of four cases (1A), (1B), (2A), and (2B). For cases (1A) and (2A) the nonlinear solver converged to the target growth state in a single load increment, and for (1B) and (2B) the solver took two increments of equal arc-length.

The radial displacement distribution along the deformed radial coordinate for these four cases is shown in Fig. 5 with the deformation magnitude contour at the target grown state shown as an inset. In all four cases there is excellent agreement between the present seven-parameter shell model and the solid-shell model by Zheng et al. [37]. Due to the radially varying metric tensor of the annulus, $\boldsymbol{G} = 1\boldsymbol{g}_r \otimes \boldsymbol{g}_r + r^2\boldsymbol{g}_\theta \otimes \boldsymbol{g}_\theta + 1\boldsymbol{g}_z \otimes \boldsymbol{g}_z$, even a spatially constant growth law, as in (1) with $g_r = g_\theta = 1.35$, leads to material fibres with varying free lengths along the radial direction (incompatible growth). In regions where the ensuing internal compressive stresses exceed a critical threshold, the annulus buckles out-of-plane to release membrane energy into bending energy. Put differently, the change in free material lengths due to growth changes the free metric tensor of the surface, which no longer corresponds to the metric of a flat annulus but a curved monkey saddle. Due to the finite thickness of the annulus, this difference in metric tensor is first accommodated by membrane stretching, but beyond a critical value of growth is accommodated at lower energetic cost through out-of-plane bending into a saddle shape. As a result, the four target growth magnitudes (1A), (1B), (2A), and (2B) specified by Zheng et al. [37] all lead to statically unstable flat equilibria as noted in Fig. 5a–d. The number of negative eigenvalues in the tangent stiffness matrix for these four flat equilibria exceeds 300 in all cases, demonstrating the high degree of instability of these flat deformations at the target growth magnitude. The next section will study the bifurcation behaviour of the growing annulus in more detail.

4.2. Out-of-plane buckling of a growing annulus

The loss of stability of the flat deformation shape of the growing annulus can be studied efficiently and robustly using the stability framework outlined in Section 3. A validation of the framework in predicting instabilities of a growing bilayer annulus is presented in Appendix B, showing excellent agreement with the results by Jin et al. [60].

The stability analysis of the growing annulus previously introduced in Section 4.1 is now shown in detail in Fig. 6 for two different scenarios. The first model, illustrated in Fig. 6a, corresponds to case (1A) above but with a parametrised growth law $\boldsymbol{F}_\mathrm{g}(\lambda_\mathrm{g}) = \mathrm{diag}(1 + \lambda_\mathrm{g}, 1 + \lambda_\mathrm{g}, 1)$ and a higher fidelity mesh (29 radial nodes and 280 circumferential nodes arranged into 490 25-noded shell elements). The equilibrium diagram in Fig. 6a is plotted as the growth factor λ_g *vs.* the thickness-normalised out-of-plane displacement w/h at point $(x, y) = (-R_\mathrm{o}, 0)$, where the maximum or minimum hump of the monkey saddle is defined to occur. The plot shows how the originally flat $(w/h = 0)$ fundamental state loses stability via a supercritical pitchfork bifurcation for a critical growth factor $\lambda_\mathrm{g}^* = 0.137 \times 10^{-5}$ and bifurcates into a three-lobed monkey saddle ($\max(w/h)$ or $\min(w/h)$ at $(x, y) = (-R_\mathrm{o}, 0)$).

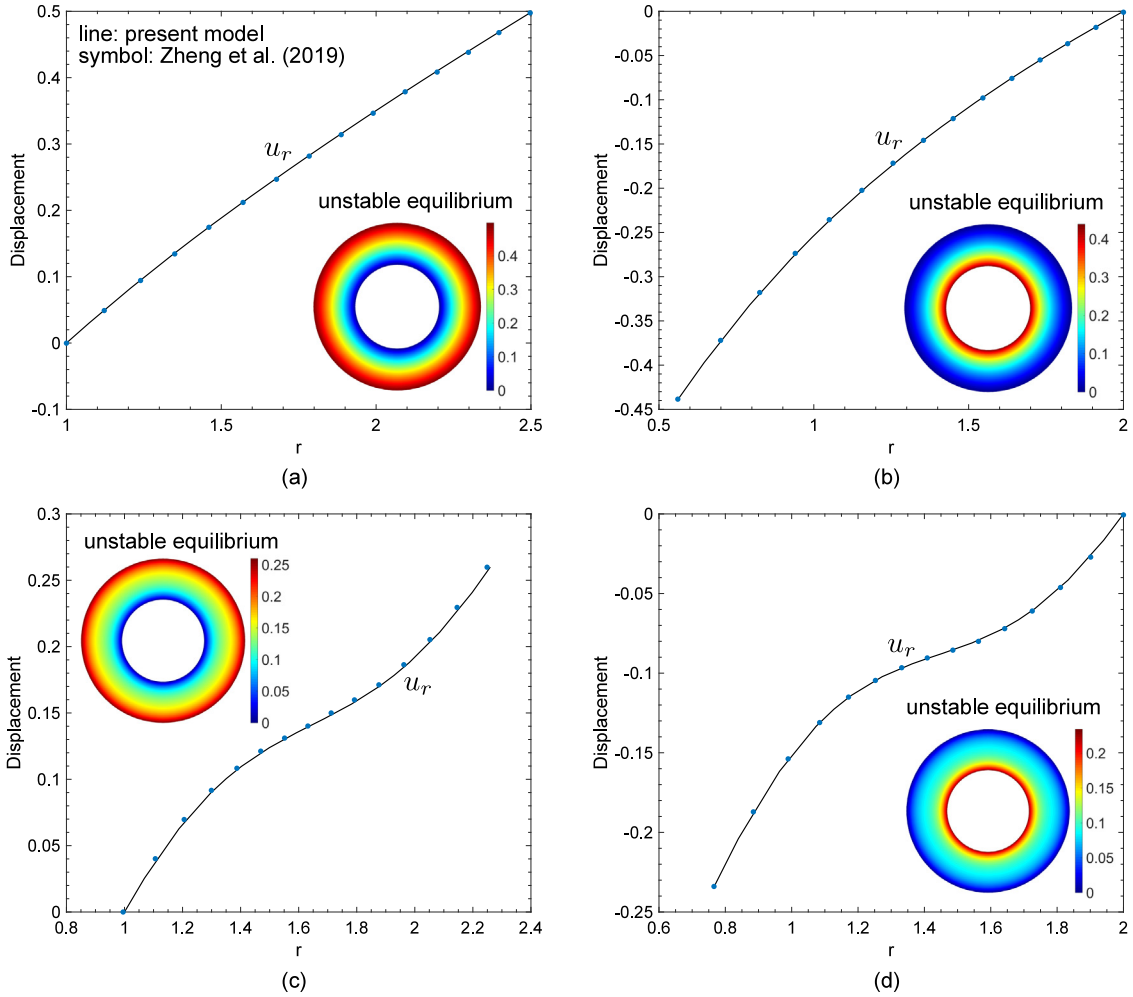

Fig. 5. Variation of the radial displacement along the deformed radial coordinate of the thin annulus for the four different growth laws described in the text. Plot (a) corresponds to case (1A); plot (b) to case (1B); plot (c) to case (2A); and plot (d) to case (2B). The present model closely matches the results by Zheng et al. [37]. The inset contours show the final (flat) deformation mode after growth with the colour contour representing the deformation magnitude. For all cases, these flat states are statically unstable.

Hence, the critical growth factor is five orders of magnitude smaller than the target growth factor $\lambda_g = 0.35$ prescribed by Zheng et al. [37], which explains the large number of negative eigenvalues in the tangent stiffness matrix for the flat state at $\lambda_g = 0.35$. Indeed, even the bifurcated three-lobed monkey saddle loses stability at a bifurcation point with $\lambda_g < 2 \times 10^{-5}$.

The second model, shown in Fig. 6b–d, maintains the geometry and material properties of the previous model but clamps the inner edge of the annulus (all seven parameters of the shell element are constrained). The annulus is now discretised with 33 radial nodes and 320 circumferential nodes that are assembled into 640 25-noded shell elements. To reflect a typical edge growth scenario, the growth law varies exponentially in the radial direction, *i.e.* $\boldsymbol{F}_g(r, \lambda_g) = \text{diag}(1 + \lambda_g e^{10(r-2)}, 1 + \lambda_g e^{10(r-2)}, 1)$ where $R_i < r < R_o$ is the radial position of the undeformed material points. Fig. 6b shows the equilibrium manifold of w/h *vs.* λ_g with w/h taken as the maximum out-of-plane displacement of the annulus. In addition, Fig. 6c–d show deformation mode shapes corresponding to the points A–C and a–c highlighted in Fig. 6b. Once more, the flat fundamental state loses stability at a supercritical pitchfork bifurcation and transitions into a four-lobed monkey saddle (see Fig. 6c-1). This lower stable branch in Fig. 6b then loses stability at a secondary bifurcation (point B) and the corresponding eigenvector in Fig. 6c-2 reveals this to be a period doubling bifurcation (eight upwards/downwards lobes in the critical eigenvector). The

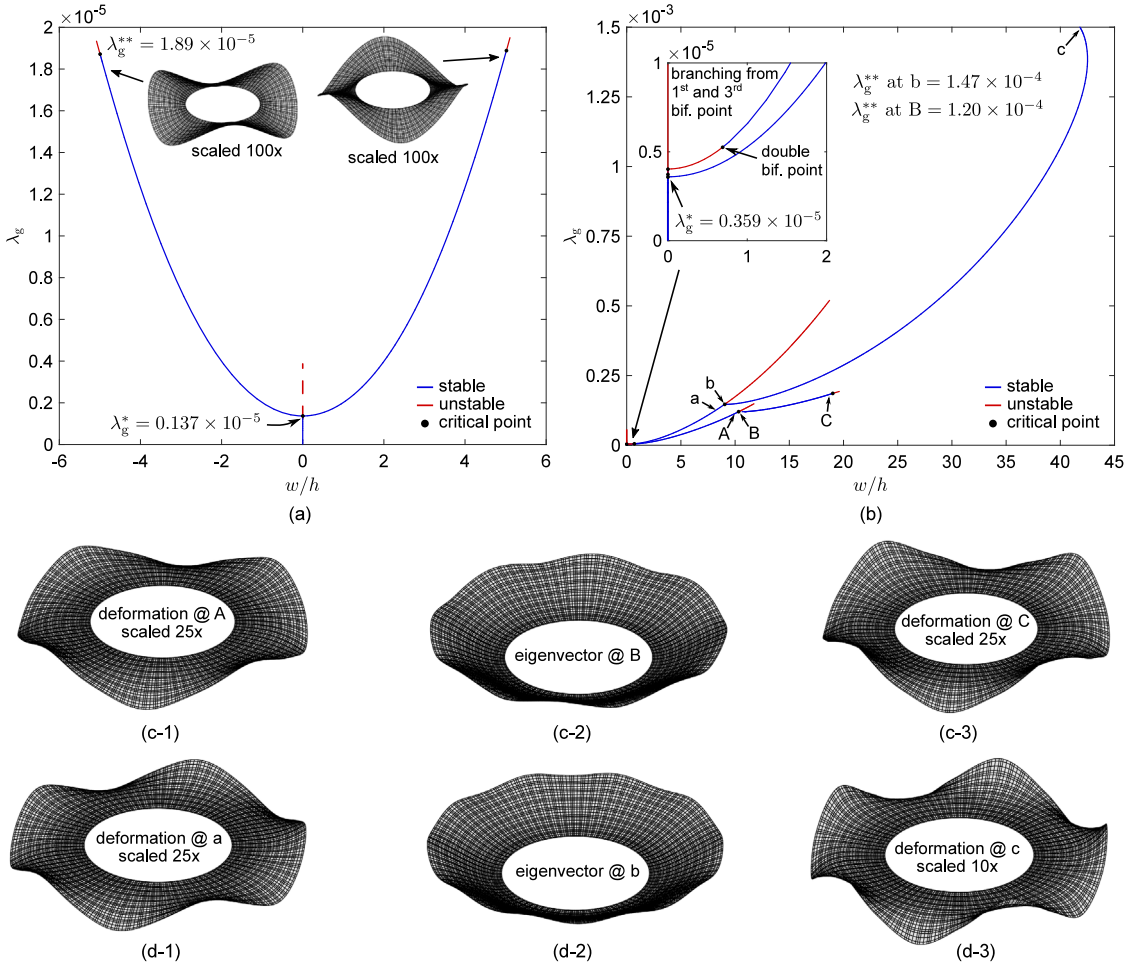

Fig. 6. Supercritical pitchfork bifurcation of a growing annulus from a flat state into a monkey saddle. (a) Annulus with pinned inner edge and spatially uniform growth law. (b) Annulus with clamped inner edge and spatially varying exponential growth law. (c,d) Mesh deformation plots of key points A–C and a–c highlighted in (b). In all deformation plots the grid lines correspond to nodal lines of the discretisation mesh.

secondary undulations from the period doubling bifurcation are visible in Fig. 6c-3 before this deformation mode too loses stability.

Interestingly, the equilibrium branch bifurcating from the third critical point on the flat fundamental path is initially unstable but stabilises at a compound (double) bifurcation point to form an alternative stable equilibrium path (see inset in Fig. 6b). This additional equilibrium path corresponds to a five-lobed monkey saddle (see Fig. 6d-1) and always maintains a higher growth factor λ_g for the same out-of-plane displacement w/h. This upper stable branch in Fig. 6b also loses stability at a period doubling bifurcation (point b) with ten upwards/downwards lobes in the critical eigenvector of Fig. 6d-2. The equilibrium branch that bifurcates from point b in Fig. 6b is then stable over an extended period of growth factor with the deformation shape shown in Fig. 6d-3.

These relatively rudimentary examples highlight the importance of tracking stability properties throughout a quasi-static morphoelastic analysis. It may seem tempting to disregard quasi-static analyses entirely because mode changes at instabilities would naturally occur when using a dynamic analysis. However, especially the second example based on the exponential growth law shows that even for relatively simple problems, incompatible growth readily leads to multi-stable morphologies that would be difficult to untangle and isolate if the shell were allowed to dynamically snap when stability is first lost. Indeed, the first and third bifurcation points on the fundamental path of the second example (see inset in Fig. 6b) are very closely spaced suggesting that small deviations in the initial

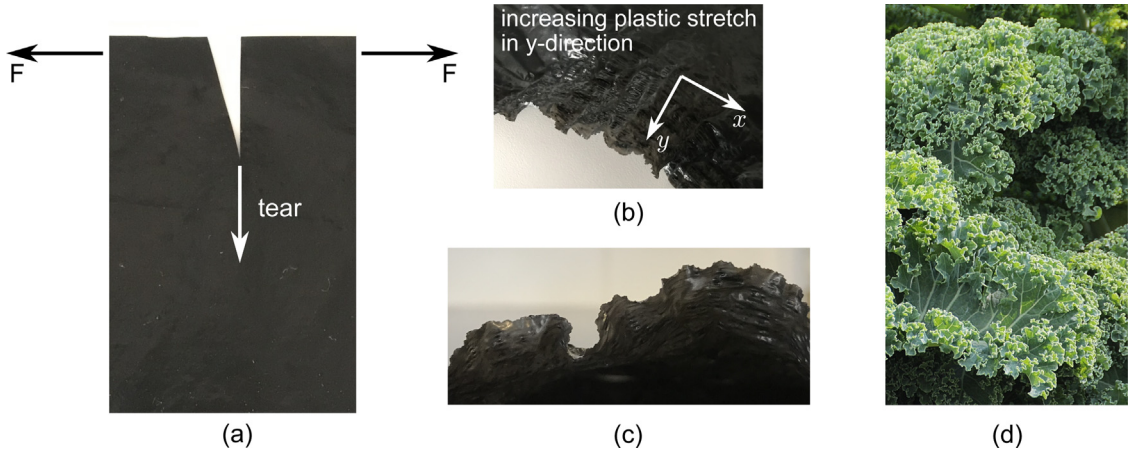

Fig. 7. A thin plastic sheet that is torn along an initial notch as shown in (a) develops a fractal wrinkling pattern along the torn edge due to the strongly increasing plastic stretch towards the edge as depicted in (b,c). The same fractal pattern is also observed in many growing biological tissues such as the leaves of common kale (*Brassica oleracea var. sabellica*) shown in (d).

conditions could lead to one mode (four- or five-lobed monkey saddle) being preferred over the other. As shown in the following sections, this scenario of multi-stability triggered by consecutive and closely spaced bifurcations from a fundamental state occurs for various geometries and growth laws, and may therefore be a general mechanism by which different morphologies evolve from nearly identical starting conditions.

4.3. Fractal wrinkling at a growing edge

Fractal wrinkling patterns at free edges have been observed in diverse scenarios ranging from growing leaves to torn plastic sheets [5] (see, *e.g.*, Fig. 7). The underlying mechanics of this pattern formation is driven by spatially varying changes to the original surface metric as a result of plastic deformation or internal growth [3,61,62].

In the case of a plastic sheet torn along an initial notch (shown in Fig. 7a–c) the induced plastic stretch is maximum at the torn edge and decreases rapidly to zero in the direction perpendicular to the edge (denoted as the y-axis in Fig. 7b). The length of a differential line element on the torn surface is given by $\mathrm{d}l^2 = f(y)^2\mathrm{d}x^2 + \mathrm{d}y^2$, where $f(y)$ describes the ratio of plastically strained differential length at position y to the initial length prior to tearing. The metric tensor induced by tearing the sheet is thus given by $\boldsymbol{G} = f(y)^2\boldsymbol{e}_x \otimes \boldsymbol{e}_x + 1\boldsymbol{e}_y \otimes \boldsymbol{e}_y$ with $f(y)$ tending to unity far from the edge (no plastic deformation) and increasing convexly towards the torn edge [3]. In general, different tearing velocities, material properties, and sheet dimensions lead to different metric functions $f(y)$, and thus different wrinkling patterns. For any surface with the above metric tensor, the associated Gaussian curvature is $K(y) = -1/f \cdot (\mathrm{d}^2 f/\mathrm{d}y^2)$ [62], which in the present case is always negative as $f(y) > 1$ ($f(y)$ is a ratio of lengths) and $\mathrm{d}^2 f/\mathrm{d}y^2 > 1$ ($f(y)$ is convex). The hyperbolic metric of the torn sheet therefore describes saddle-like configurations, and for sufficiently high plastic stretching or sufficiently low bending rigidity, the originally flat sheet buckles out-of-plane to conform to this saddle curvature. If the metric $f(y)$ leads to increasingly negative Gaussian curvature towards the free edge, a cascade of saddles upon saddles may form [62].

In Section 2.3 we mentioned the similarities in modelling plasticity and growth based on the multiplicative decomposition of the deformation gradient tensor. Hence, it is no surprise that the fractal wrinkles in a plastically deformed sheet are similar to those observed in certain growing biological tissues (compare Fig. 7c to d). To model fractal wrinkling at the free edge of a growing tissue, we consider an initially flat, rectangular sheet of length $L = 12\,\mathrm{cm}$ in the x-direction, $W = 3\,\mathrm{cm}$ in the y-direction, and a thickness of $h = 0.02\,\mathrm{cm}$ with one edge at $y = 3\,\mathrm{cm}$ clamped (all dofs constrained). The sheet is discretised into 249×61 nodes in the x- and y-directions, respectively, which are then assembled into 930 25-noded spectral elements. The element distribution in the y-direction is logarithmic with a bias of finer density towards the free edge. The shear modulus of the sheet is taken as $\mu = 4 \times 10^3\,\mathrm{N/cm^2}$ and the bulk modulus as $K = 4 \times 10^5\,\mathrm{N/cm^2}$. A one-dimensional and spatially varying growth law is defined in the global Cartesian coordinate system $\boldsymbol{F}_\mathrm{g}(y, \lambda_\mathrm{g}) = \mathrm{diag}(g_x(y, \lambda_\mathrm{g}), 1, 1)$, where $g_x(y, \lambda_\mathrm{g})$

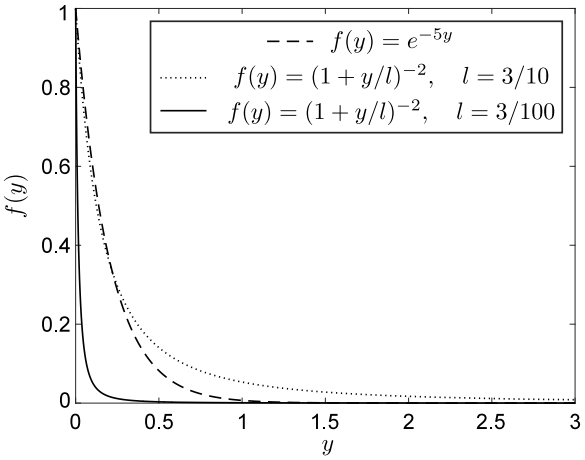

Fig. 8. Different exponential and power law functions used to model longitudinal edge growth in an initially flat sheet. Only the sharp power law represented by the solid line leads to a fractal wrinkling pattern at the free edge.

describes longitudinal growth in the x-direction with greatest magnitude (parametrised through growth factor λ_g) at the free edge, $y = 0\,\text{cm}$, and smallest magnitude $g_x(y, \lambda_g) \to 1$ at the clamped edge, $y = 3\,\text{cm}$.

In the following, two different types of growth law are assumed for $g_x(y, \lambda_g)$, where the x-direction metric always increases convexly towards the free edge. The first case is inspired by Marder et al. [3] and assumes exponential growth towards the free edge with $g_x(y, \lambda_g) = 1 + \lambda_g e^{-5y}$. For clarity, the exponential function is visualised in Fig. 8 by the dashed line. Qualitatively identical results can also be produced by using power law growth of the form $g_x(y, \lambda_g) = 1 + \lambda_g(1 + y/l)^{-a}$ with $a = 2$ and a characteristic length-scale parameter of $l = W/10\,\text{cm}$ ($W = 3\,\text{cm}$ is the width of the sheet in the y-direction). The power law function is visualised in Fig. 8 by the dotted curve and is almost coincident to the previous exponential law towards the free edge ($y = 0\,\text{cm}$). The second case modelled herein shortens the characteristic length-scale parameter of the power law to $l = W/100\,\text{cm}$ to produce a sharper increase in longitudinal growth towards the free edge of the sheet (see the solid curve in Fig. 8). This second growth law leads to (i) a significantly greater mismatch between the free lengths of grown material fibres over a specific length scale close to the free edge; and (ii) a more rapidly scaling negative Gaussian curvature of the associated free surface metric towards the edge.

These two scenarios of more benign exponential growth (or equivalent power law growth with $l = W/10\,\text{cm}$) and the steeper power law growth ($l = W/100\,\text{cm}$) are now studied in turn. Fig. 9a shows an equilibrium manifold for the exponential growth law in terms of the thickness-normalised out-of-plane displacement w/h at one free corner of the sheet *vs.* the growth factor λ_g. As shown in the inset of Fig. 9a the growing sheet initially remains flat ($w/h = 0$) but this flat equilibrium state loses stability at a supercritical pitchfork bifurcation. In fact, there are two closely spaced bifurcation points on the fundamental path. The eigenvector of the first critical point corresponds to one full wave forming at the free edge (see Fig. 9b-A), while the eigenvector of the second critical point corresponds to 1.5 waves (see Fig. 9b-a). Branch switching from these two bifurcation points leads to the two intertwined post-critical equilibrium branches shown in Fig. 9a. Both of these paths are seen to weave backwards and forwards with alternating negative and positive values of w/h. The deformation modes in Fig. 9b show that the two post-critical equilibrium paths describe pattern formation sequences into increasing number of edge waves and increasingly smaller wavelength. The post-critical equilibrium path branching from the first critical point corresponds to mode shapes that are left–right symmetric (crests or valleys at both free corners, see points A–D in Fig. 9b), whereas the post-critical equilibrium path branching from the second critical point corresponds to mode shapes that are left–right antisymmetric (crest at one free corner and valley at the other, see points a–d in Fig. 9b). The first post-critical path is initially stable (see inset in Fig. 9a) such that the flat sheet buckles onto this path to begin with. As the growth factor λ_g increases further both equilibrium paths exchange stability by undergoing a series of re- and destabilisations at additional bifurcation points. As shown in Fig. 9a, the two post-critical paths are connected by unstable segments between bifurcation points. Hence, as the growth factor λ_g increases the sheet successively snaps

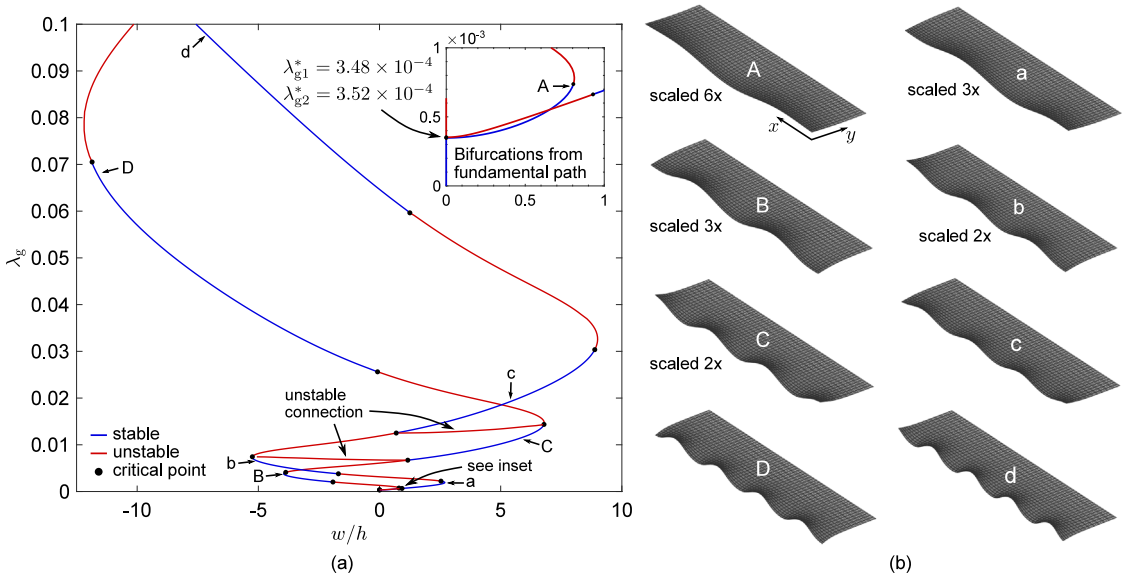

Fig. 9. Wrinkling at a free edge of a flat sheet due to exponential edge growth. Two pitchfork bifurcations (critical points λ_{g1}^* and λ_{g2}^*) that branch from the flat fundamental state are intertwined and correspond to left–right symmetric and antisymmetric wrinkling modes. (a) The equilibrium paths of growth factor λ_g *vs.* the thickness-normalised out-of-plane displacement w/h at one free corner of the sheet; (b) Deformation plots of different points marked on the equilibrium curves in (a).

between the left–right symmetric and left–right antisymmetric undulation modes, all the while increasing the wave number and decreasing the wavelength at the free edge.

The two intertwined equilibrium paths that describe mode changes into greater and greater wave numbers are at first sight reminiscent of *homoclinic snaking* [63] that governs the pattern formation in axially compressed cylinders [64,65]. However, homoclinic snaking describes a process whereby an initially localised post-critical solution multiplies through a series of limit point instabilities into a periodic waveform. Crucially, the wavelength of the original localised cell remains constant and does not modulate as the pattern multiplies. Furthermore, in snaking the forcing parameter oscillates within a bounded pinning region around the so-called *Maxwell load* [66] where the pre-critical and periodic post-critical modes have equal energy. As none of these characteristics are observed in the present case, the pattern formation must be governed by different mechanics. Here, a useful analogy can be made to an initially straight beam resting on an elastic stiffening foundation. If we model the infinitesimal longitudinal line of the sheet at $y = 0\,\text{cm}$ as a 1D beam, then the rest of sheet acts as an equivalent restraining foundation because the edge is defined to grow the most. With increasing growth factor λ_g, the effective restraint, and hence the stiffness of the equivalent foundation, increases as the spatial mismatch in growth is proportional to λ_g. As is well known from buckling of a beam on an elastic foundation, the buckling wavelength scales inversely with the foundation stiffness, and we should therefore expect a shortening of the wavelength for increasing λ_g. This is indeed what we observe in Fig. 9.

Another trend in the equilibrium manifold of Fig. 9a is that the two post-critical paths spread out both on the horizontal (w/h) and vertical (λ_g) axes. Hence, the incremental change in growth factor ($\Delta\lambda_g$) between two successive wave numbers increases, and the out-of-plane deformation magnitude of each wave ($|w/h|$) also increases significantly with increasing λ_g. Therefore, as growth proceeds the sheet increasingly accommodates the extra length at the free edge through out-of-plane deformation rather than favouring further shortening of the buckling wavelength. Indeed, this trend of accommodating differential edge growth predominantly through out-of-plane deflection continues well beyond the ordinate range $\lambda_g < 0.1$ shown in Fig. 9a. An extension of the present analysis up to $\lambda_g = 2$ leads to large out-of-plane deflections of $|w/h| > 35$ with little increase in the wave number, and ultimately to self-contact of individual wrinkles at the free edge. Hence, these findings corroborate previous observations by Marder et al. [3] that a benign exponential or power law growth function towards a free edge does not lead to fractal wrinkling patterns.

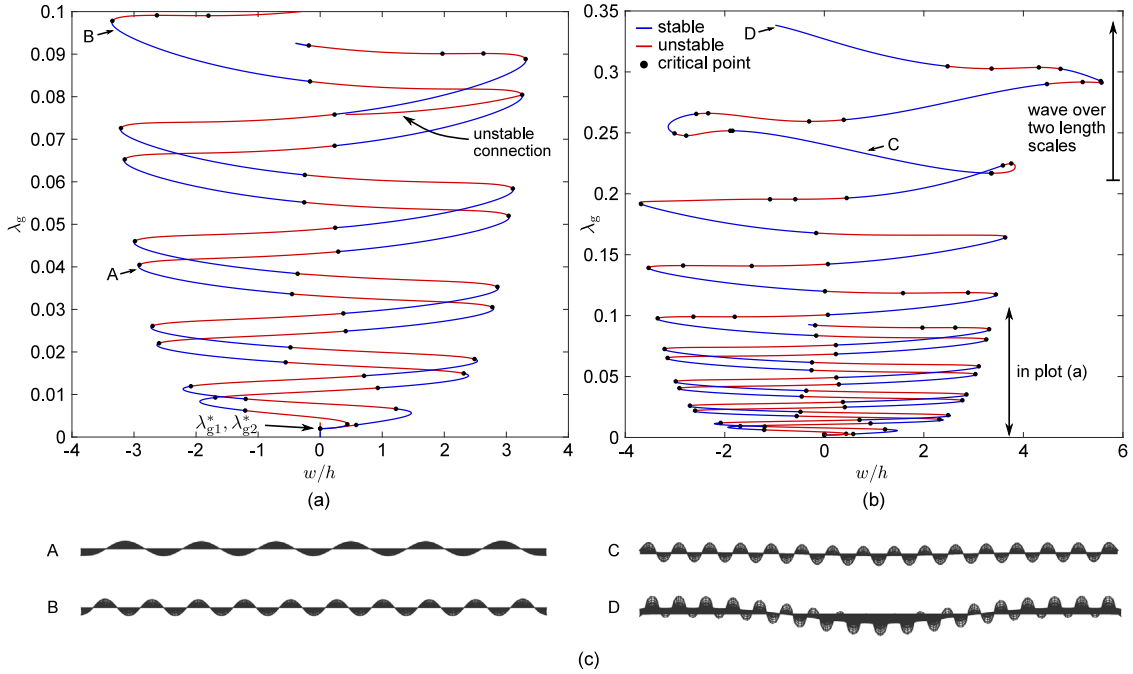

Fig. 10. Wrinkling at a free edge of a flat sheet due to steeper power law edge growth. Two pitchfork bifurcations (critical points $\lambda^*_{g1} = 1.97 \times 10^{-3}$ and $\lambda^*_{g2} = 1.99 \times 10^{-3}$) that branch from the flat fundamental state are intertwined and correspond to left–right symmetric and antisymmetric wrinkling modes. (a) and (b) show the equilibrium paths of growth factor λ_g *vs.* the thickness-normalised out-of-plane displacement w/h at one free corner of the sheet. (a) Shows the region of growth factor $\lambda_g < 0.1$ where wrinkling occurs over one length scale, whereas (b) shows an extended equilibrium manifold $\lambda_g < 0.35$ with wrinkling occurring over two length scales for $\lambda_g \gtrapprox 0.2$. (c) Deformation plots of different points marked on the equilibrium curves in (a) and (b) with all out-of-plane displacements amplified by a factor of 3.

Fig. 10a shows the equilibrium manifold for steeper power law growth ($l = W/100\,\text{cm}$) in terms of the thickness-normalised out-of-plane displacement w/h at one free corner of the sheet *vs.* the growth factor λ_g. As discussed for the exponential growth law, we observe two post-critical equilibrium paths that branch from closely spaced bifurcation points on the fundamental equilibrium path of the flat sheet ($w/h = 0$). The two post-critical paths are again intertwined, connected by unstable segments, and describe left–right symmetric and left–right antisymmetric wrinkling patterns of increasingly shorter wavelength as the growth factor λ_g increases. Contrary to the exponential growth law in Fig. 9a, the out-of-plane deformation w/h grows much slower with increasing λ_g; for example, when $\lambda_g \approx 0.1$ we have $\max(w/h) \approx 3.5$ in Fig. 10a compared to $\max(w/h) \approx 12$ in Fig. 9a. Furthermore, a greater number of back-and-forth oscillations occur in the two equilibrium paths for the steeper power law, indicating more transitions to shorter wavelengths over the same range of growth factor. Indeed, the deformation modes shown for points A and B in Fig. 10c visually highlight the greater number of undulations at the edge of the sheet compared to the same level of growth in Fig. 9.

Above a critical threshold of steep power law growth the wrinkling behaviour of the sheet changes qualitatively. Fig. 10b extends the equilibrium path of the left–right symmetric wrinkling pattern to the range $\lambda_g < 0.35$. For $\lambda_g \gtrapprox 0.2$ the equilibrium path breaks the previous regular pattern of weaving backwards and forwards and significantly increases the out-of-plane displacement w/h by initiating a second wave at a longer length scale. As shown in the deformation modes for points C and D in Fig. 10c, the transition in behaviour above $\lambda_g \approx 0.2$ freezes the wavelength of the existing wrinkling pattern and an additional longer wavelength undulation forms.

For the steeper power law growth we therefore have a scenario where the sheet initially accommodates the growing length of the free edge by forming undulations of shorter and shorter wavelength. At a certain threshold of growth, a further reduction of the wavelength becomes energetically more expensive than forming a secondary longer wavelength undulation. Returning to the analogy of the beam on an elastic foundation, energy minimisation of the

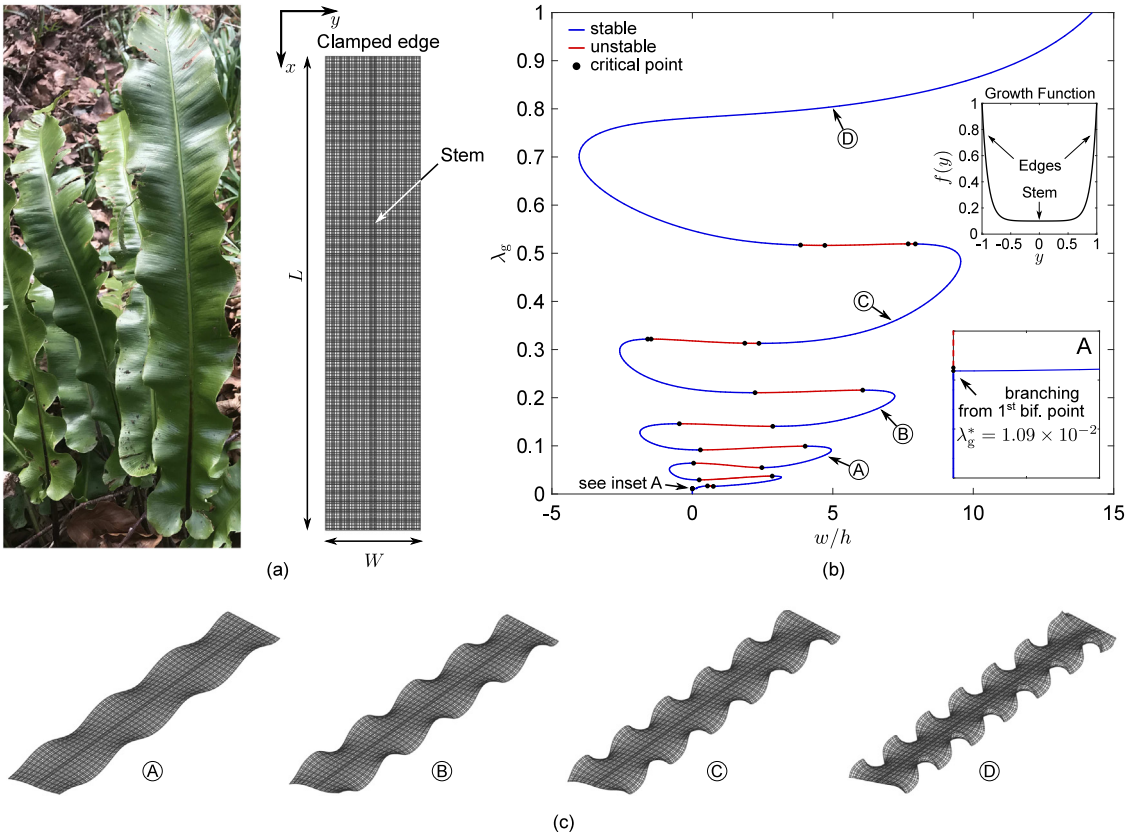

Fig. 11. (a) Edge wrinkling of *Asplenium scolopendrium* or hart's-tongue fern is modelled using a long strip with a stiffer and thicker central section to account for the stem. Exponentially increasing planar growth towards the long edges is applied, producing the morphoelastic equilibrium manifold in (b) with a bifurcation at λ_g^*. The out-of-plane deflection w/h at a free corner of the strip weaves backwards and forwards with increasing growth factor λ_g. As growth proceeds, both the number of waves along the edge and their out-of-plane deflection magnitude increases; depicted in (c).

foundation initially drives the mechanics by reducing the wavelength and keeping overall out-of-plane deformations small. The reduction in wavelength comes at the expense of having a highly curved free edge with increasing levels of bending energy. The longitudinal wavelength at the free edge thus continues to shorten with increasing growth factor until the longitudinal curvature is sufficiently large and energetically expensive that a transition in behaviour occurs. It is now more favourable to freeze the existing wavelength of the smaller length scale and to accommodate additional differential growth of the edge through global out-of-plane deflections at a greater length scale.

4.4. Exponential edge growth in leaves

To put exponential edge growth into context we consider the leaves, or so-called fronds, of *Asplenium scolopendrium*, also known as hart's-tongue fern (see Fig. 11a). The edges of the undivided fronds of *Asplenium scolopendrium* are generally wrinkled and display a variety of different morphologies—from shallow sinusoidal waves to pronounced crinkles that are close to self-contact. A single frond of *Asplenium scolopendrium* is here modelled by a long strip of length $L = 10\,\text{cm}$ in the x-direction and width $W = 2\,\text{cm}$ in the y-direction with a stiffer central section of width $W_{\text{stem}} = 0.1\,\text{cm}$ to account for the stem (see Fig. 11a). The central stem has a thickness of $h_{\text{stem}} = 0.1\,\text{cm}$ and the leafy part of the frond outside of the stem has a thickness of $h = 0.05\,\text{cm}$. Based on typical values of plant materials [67], the woody stem has a stiffer shear modulus of $\mu = 1 \times 10^5\,\text{N/cm}^2$ with a bulk modulus of $K = 1 \times 10^7\,\text{N/cm}^2$, and the leafy part of the frond has a more compliant shear modulus of $\mu = 1 \times 10^4\,\text{N/cm}^2$ with a bulk modulus of $K = 1 \times 10^6\,\text{N/cm}^2$.

The rectangular frond is discretised into 201 × 53 nodes in the x- and y-directions, respectively, and the nodes are then assembled into 650 25-noded spectral elements (a one-element wide strip of 25-noded elements is used for the stem). The lateral edge at $x = 0\,\text{cm}$ is clamped (all dofs constrained) with all other portions of the frond unconstrained. A planar growth tensor of the form $\boldsymbol{F}_g(y, \lambda_g) = \text{diag}(g(y, \lambda_g), g(y, \lambda_g), 1)$ is defined in a local Cartesian coordinate system $\{\boldsymbol{e}_1, \boldsymbol{e}_2, \boldsymbol{e}_3\}$, where $\boldsymbol{e}_1$ and $\boldsymbol{e}_2$ lie in the plane of the undeformed frond parallel to the global x- and y-direction, respectively, and $\boldsymbol{e}_3$ is normal to the frond's undeformed surface. The growth law thus causes length- and width-wise growth with the growth magnitude varying in the width direction parametrised by the growth factor λ_g. The growth function is defined as $g(y, \lambda_g) = 1 + \lambda_g \left(0.9e^{10(|y|-1)} + 0.1\right)$, where the exponential term takes a value of 1 at either long edge of the frond ($y = \pm 1\,\text{cm}$) and a smaller value of 0.100 at the stem ($y = 0\,\text{cm}$). The exponential function is shown for reference in Fig. 11b and mimics, in a more continuous manner, the discrete differential edge growth assumed by Zheng et al. [37] and Eskandari and Kuhl [68] for *Rumex crispus* leaves.

The equilibrium manifold in Fig. 11b shows the now familiar behaviour of differential edge growth discussed in the previous section. The figure plots the thickness-normalised out-of-plane displacement at a free corner of the strip (w/h) against the growth factor (λ_g). As the frond begins to grow it initially remains flat ($w/h = 0$) but this fundamental state loses stability at a supercritical pitchfork bifurcation (see inset A in Fig. 11b) where the two edges of the strip begin to wrinkle. The wrinkling waves at the two edges are antisymmetric about the stem (see point A in Fig. 11c) where a crest at the left edge is mirrored by a valley at the right edge, and *vice versa*. A left–right symmetric bifurcation mode also exists—branching from the third critical point on the fundamental path—but this mode is unstable throughout for the geometry and material properties considered here.

The left–right antisymmetric wrinkling mode provides an important counterexample to the claim by Zheng et al. [37]—studying growth-induced edge wrinkling of a similarly sized and shaped *Rumex crispus* leaf—that: "Because of the symmetry of the geometry and growth, the deformation caused by the mass growth is symmetrical, too". This statement is not true in general because bifurcations inherently break symmetry groups of the system, be they symmetry planes about the mid-plane (buckling phenomena in general) or, in this particular case, an in-plane symmetry group.

The post-critical equilibrium path in Fig. 11b weaves backwards and forwards with each turn increasing the number of waves on the edge and shortening the wavelength (see the progression from point A to point D in Fig. 11c). In addition, the out-of-plane deflection magnitude ($|w/h|$) also increases markedly as growth proceeds. The four deformation shapes in Fig. 11c show the evolution of the antisymmetric edge wrinkling modes from shallow sinusoidal and long wavelength (point A) to highly undulated and short wavelength (point D). Hence, the different wave shapes and wavelengths observed at the edges of *Asplenium scolopendrium* can be attributed to the level of edge growth, which may vary from leaf to leaf or even spatially within a single leaf. The greater the growth factor for a given edge growth law, or alternatively, the steeper the gradient of differential growth towards an edge, the more pronounced the wrinkles/crinkles that occur at the edge.

4.5. Trumpeting of a daffodil corona

Plants of the genus *Narcissus* feature recognisable flowers with petal-like tepals arranged around a trumpet-shaped corona (see Fig. 12a). While the blooming of flower petals is modelled in Section 4.6, here we consider growth of the trumpet-shaped corona of a generic *Narcissus* plant. We show that exponentially increasing planar growth towards one end of a cylindrical tube first causes the growing end to "trumpet" outwards before buckling instabilities induce transitions to a wavy edge that closely resembles the shape of a *Narcissus* corona.

The corona is modelled as an initially ungrown cylindrical tube of length $L = 2\,\text{cm}$, radius $R = 1\,\text{cm}$ and thickness $h = 0.02\,\text{cm}$ with one end fully clamped (all dofs constrained) and the other end unconstrained (see Fig. 12b). The assumed material properties are shear modulus $\mu = 4 \times 10^3\,\text{N/cm}^2$ and bulk modulus $K = 4 \times 10^5\,\text{N/cm}^2$ based on typical values of plant materials [67]. The cylindrical tube is discretised into 73 axial and 248 circumferential nodes that are assembled into 1116 25-noded spectral elements. The element distribution is logarithmic in the axial direction, leading to a finer axial mesh density towards the free end (see Fig. 12b).

A planar growth deformation tensor of the form $\boldsymbol{F}_g(x, \lambda_g) = \text{diag}(g(x, \lambda_g), g(x, \lambda_g), 1)$ is defined in a local Cartesian coordinate system $\{\boldsymbol{e}_1, \boldsymbol{e}_2, \boldsymbol{e}_3\}$, where $\boldsymbol{e}_1$ and $\boldsymbol{e}_2$ lie in the plane of the tube parallel to the axial and circumferential directions, respectively, and $\boldsymbol{e}_3$ stands normal to the tube's surface. The growth law thus causes

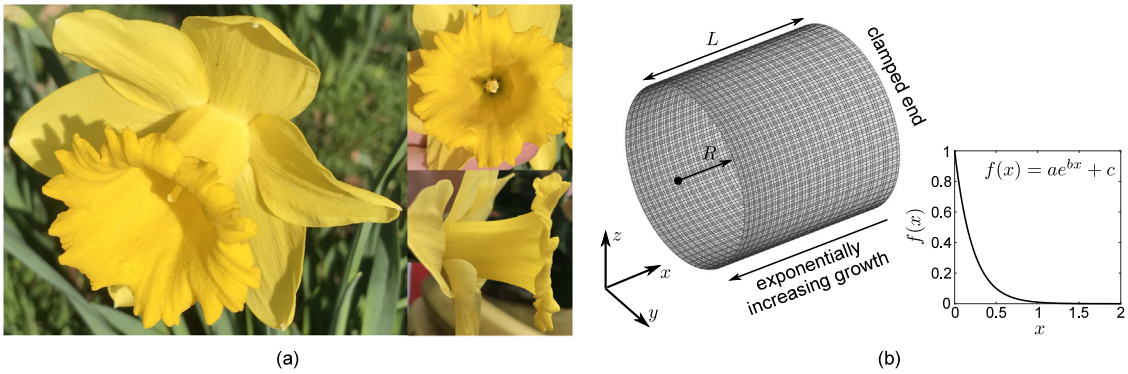

Fig. 12. (a) Images of a generic plant of the genus *Narcissus* with petal-like tepals arranged around a trumpet-shaped corona. The profile views of the corona show a rapidly increasing radius towards the free end. (b) Growth of the corona is modelled by taking an ungrown cylindrical tube that is clamped at one end that undergoes exponentially increasing planar growth (axial & circumferential) towards the other end.

axial elongation and radial dilation of the tube that are both defined to vary along the tube's length, with an overall magnitude parametrised by the growth factor λ_g. As is evident from observing a typical daffodil (see, *e.g.*, Fig. 12a) the diameter of the corona increases gradually near the base and more rapidly towards the free end. This spatially varying growth leads to residual stresses that at some point cause buckling of the free end into a wavy pattern.

Based on the above observations, the planar growth law is defined as

$$g(x, \lambda_g) = 1 + \lambda_g \left(ae^{bx} + c\right), \tag{56}$$

where we assume $a = 1.0001020408$, $b = -4.5951198501$ and $c = -1.0204081632 \times 10^{-4}$ based on the criteria that the exponential term $f(x) = ae^{bx} + c$ satisfies $f(0) = 1$, $f(1) = 0.01$ and $f(2) = 0$ (see the growth law curve in Fig. 12b). When implemented in the defined growth deformation tensor, the growth law causes increasing radial dilation towards the free end, which is here dubbed as "trumpeting".

Fig. 13a,b show two equilibrium manifolds of the growing cylindrical tube plotted in terms of the maximum radial displacement at the free end of the tube (v/h) *vs.* the growth factor (λ_g). The equilibrium path running diagonally in blue (stable) in Fig. 13a, corresponds to the tube growing axisymmetrically into a trumpet-like shape (see Fig. 13c). This axisymmetric shape loses stability at a supercritical pitchfork bifurcation (see $\lambda_g^* = 0.246$ in inset A of Fig. 13a) and the eigenvector of this critical point features 9 circumferential waves at the free end (see point i in Fig. 13d). The addition of the signed eigenvector into the displacement field leads to two possible deformation patterns (see points ii and iv in Fig. 13d), and the corresponding equilibrium paths are denoted by the first and second branch of the pitchfork in Fig. 13a. Along both of these pitchfork paths, the magnitude of the axisymmetric trumpet mode increases alongside the wavy pattern seeded by the critical eigenvector.

Interestingly, both branches of the pitchfork reach a limit point for $\lambda_g^{**} = 1.16$ and then continue for decreasing growth factor until the two unstable segments meet close to the original bifurcation point (see inset A in Fig. 13a). Hence, the two branches of the pitchfork are connected in a closed loop, which is unlike the more common scenario of the Euler strut or the growing annulus in Fig. 6a. Also highlighted in inset A of Fig. 13a is point iii, which denotes the critical point where the two unstable segments of the pitchfork meet to form a closed loop. At point iii ($\lambda_g^{***} = 0.248$) the edge of the tube now features 8 circumferential waves (see point iii in Fig. 13d) forming a transition between the two radially inverted nine-waved modes of the two branches of the pitchfork. Point iii thus forms an additional bifurcation point with a connected equilibrium path that preserves an extra symmetry group; *i.e.* left–right symmetry in addition to the previous up-down symmetry of the nine-waved modes. The additional equilibrium path connected to point iii is highlighted in Fig. 13b with the connection shown clearly in inset B. This equilibrium path of the doubly-symmetric eight-waved mode is stable over a significant range of growth factor (shown here up to $\lambda_g = 2$) and leads to a wavy tube that closely resembles the shape of a *Narcissus* corona.

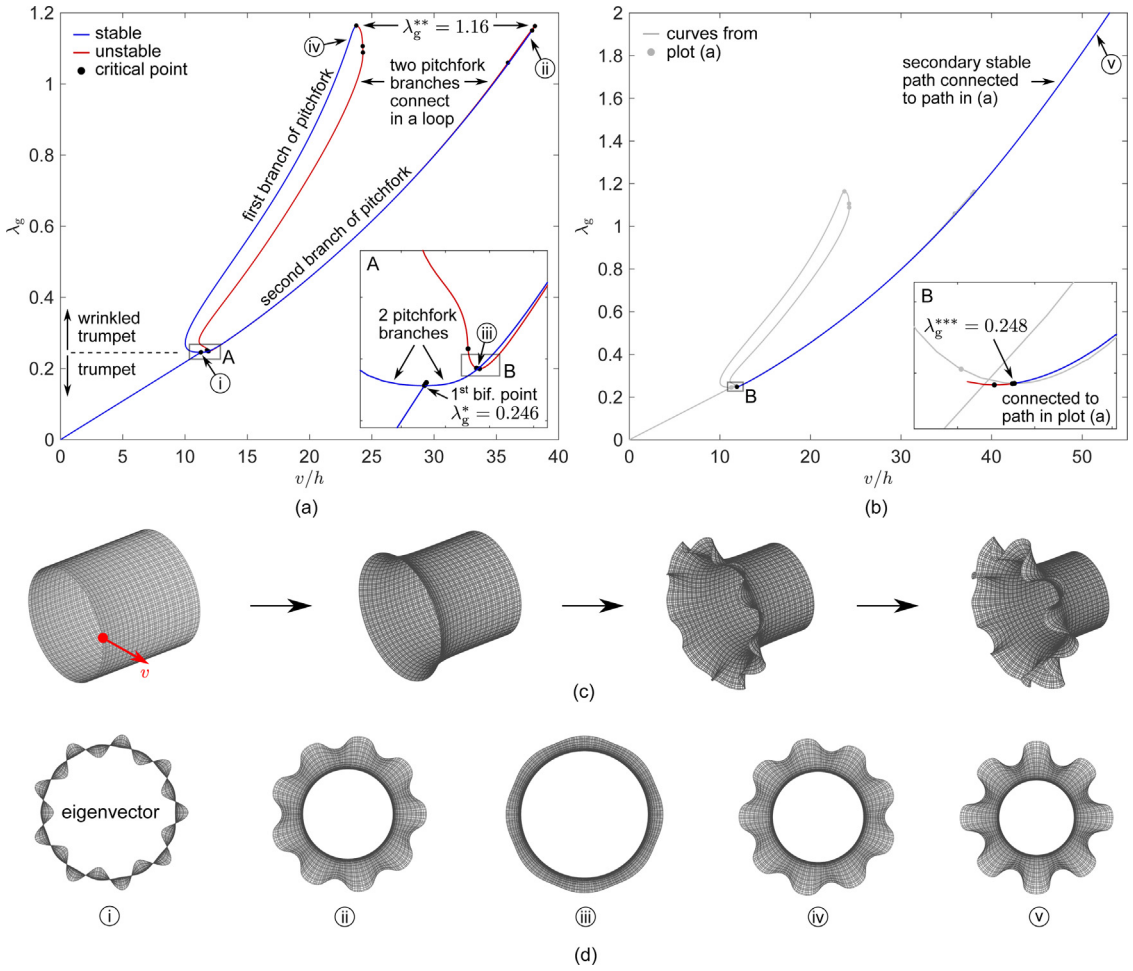

Fig. 13. (a) Equilibrium manifold in terms of maximum radial displacement v/h *vs.* growth factor λ_g of the growing tube showing a pitchfork bifurcation at λ_g^* that demarcates a trumpet-like tube from an edge-wrinkled trumpet-like tube. Apart from the wrinkled edge with 9 waves, another edge-wrinkled state with 8 waves exists with the associated equilibrium manifold depicted in (b). Subplot (c) shows the evolution of growth from cylindrical tube to trumpet and further to edge-wrinkled trumpet, while subplot (d) shows the frontal view of five different deformation states highlighted in (a) and (b).

Growth of a daffodil's corona, modelled by means of an exponentially growing tube, thus proceeds as follows (see Fig. 13c). The exponential growth law initially leads to a greater increase of the radius at the free end of the tube with an associated axisymmetric trumpet-shaped deformation. If unconstrained, each material fibre towards the free end would radially dilate more than its adjacent inwards neighbour. Compatibility of displacement (no tears or material overlap), however, means that material fibres towards the free end are increasingly placed in compression until, at a critical value of growth factor, the axisymmetric mode loses stability and a buckled wavy pattern forms. This first wavy pattern loses stability at a greater level of growth and the tube snaps via a limit point instability into an alternative pattern with fewer waves and a longer wavelength. Therefore, bending energy in the circumferential direction appears to be driving the evolution of the pattern with a reduction in circumferential bending curvature during the transition from nine waves to eight. Given the observations of the previous section on fractal patterns, it is conceivable that more pronounced exponential growth with steeper gradients towards the free end would reverse this trend, whereby membrane stretching energy due to differential growth of material fibres becomes the driving factor and the tube evolves into higher wave numbers instead.

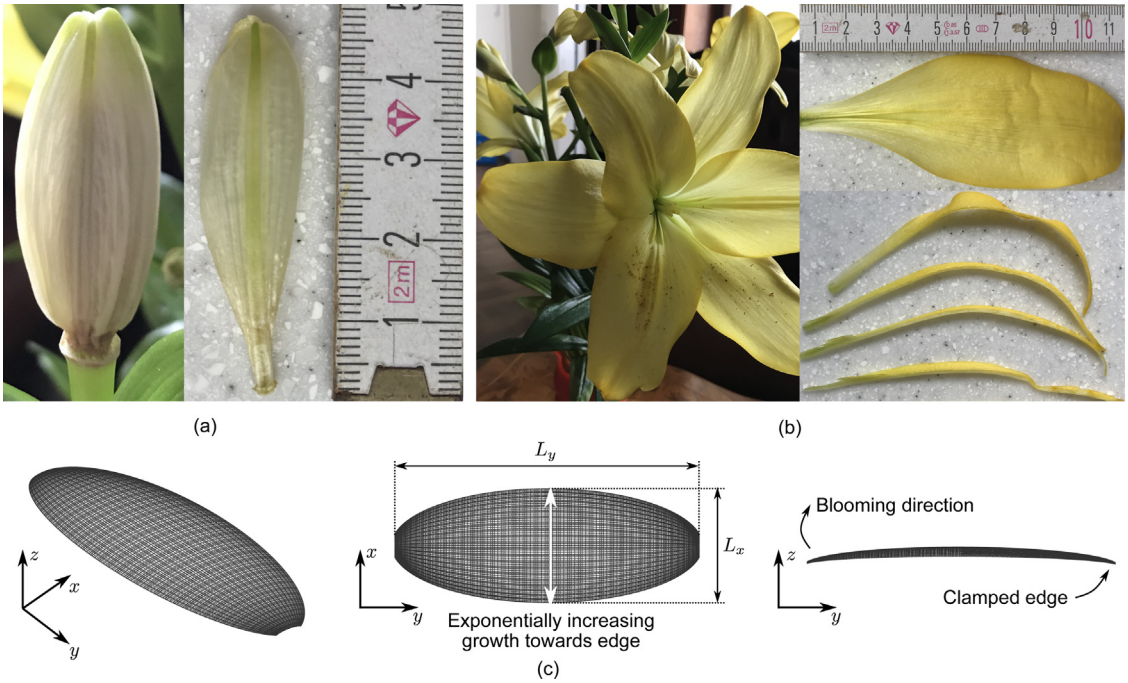

Fig. 14. (a) A closed flower bud of a yellow day lily (*Hemerocallis lilioasphodelus*) that is comprised of six petals arranged across two layers. (b) The flower bud opens up (blooms) as a result of spatially varying planar growth of each petal. Cutting a grown petal to release internal stress shows that the edges of the petal grow more than the central regions close to the midrib. (c) The blooming of a single petal is modelled by an elliptical doubly-curved shell that is clamped at one end with exponentially increasing planar growth towards the two longitudinal edges. (For interpretation of the references to colour in this figure legend, the reader is referred to the web version of this article.)

4.6. Blooming of lily buds

The blooming of lily buds has been identified to occur as a result of differential edge growth [6]. As shown for the yellow day lily (*Hemerocallis lilioasphodelus*) in Fig. 14, the unopened lily bud starts with six doubly-curved petals arranged side-by-side in 120° intervals and across two overlapping layers with each petal blooming outwards into an opened saddle shape. As can be confirmed by cutting a grown and opened petal lengthways (see Fig. 14b), the edges of a petal grow more than the central regions and this differential growth leads to a reversal of the longitudinal curvature and the opening of the lily bud. Experimental and numerical work by Liang and Mahadevan [6] shows that this phenomenon is independent of the woody midrib. When the midrib is removed from the petal, blooming occurs as before, but to a slightly different curvature as for the pristine petal.

The important role of differential edge growth in blooming of lily buds is studied here by modelling a single petal as an elliptical doubly-curved shell. Based on measurements of a single petal in the unopened bud (see Fig. 14a) the ungrown and stress-free original petal is defined to have length $L_y = 4\,\text{cm}$ and width of $L_x = 1.5\,\text{cm}$. The out-of-plane and stress-free height L_z of the petal (influencing the initial curvature) was varied in the range of $L_z = 0.1$–0.5 cm, each time leading to similar qualitative results. The model results shown here assume $L_z = 0.25\,\text{cm}$.

The geometry of the petal is based on the equation of an ellipsoid,

$$\left.\begin{aligned} x &= a\cos(\theta)\cos(\phi) \\ y &= b\sin(\theta) \\ z &= c\cos(\theta)\sin(\phi) \end{aligned}\right\} \quad \begin{aligned} &\text{for} \quad \theta \in \left[-\frac{\pi}{2} + \theta_c, \frac{\pi}{2} - \theta_c\right], \\ &\text{and} \quad \phi \in [0 + \phi_c, \pi - \phi_c]\,. \end{aligned} \tag{57}$$

In the model we assume $\theta_c = \pi/15$ to truncate the ellipsoid in the y-direction (see Fig. 14c). This allows clamping of an edge of nodes at one end (all dofs constrained) to mimic a rigid connection of the petal to the pedicel. The

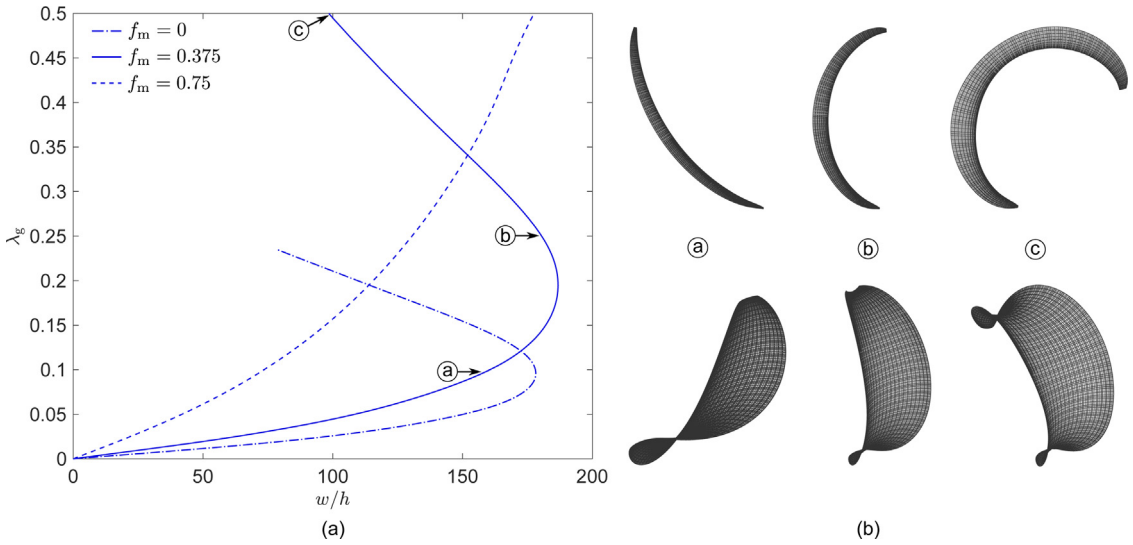

Fig. 15. (a) Equilibrium curves of thickness-normalised z-axis displacement at the free tip of the petal (w/h) *vs.* growth factor (λ_g) for three different exponential edge growth scenarios. The smaller the value of f_m, the more pronounced the degree of edge growth. (b) Deformation modes of the petal at three different points that clearly illustrate the blooming process from the originally flat configuration. Blooming leads to a reversal of the concave longitudinal curvature into a saddle shape.

variable $\phi_c = \pi/6$ truncates the petal in the x-direction such that the total angle enclosed by the petal is $2\pi/3$ rad, *i.e.* three petals connect side-by-side around the circumference of the bud. To match the defined length $L_y = 4$ cm and width $L_x = 1.5$ cm, we specify $a = 0.5L_x/\cos(\phi_c)$ and $b = 0.5L_y/\sin(\pi/2 - \theta_c)$ in Eq. (57). The variable c is defined equal to L_z. Finally, the thickness of the petal is taken as $h = 0.02$ cm with a shear modulus of $\mu = 5 \times 10^2$ N/cm^2 [6] and a bulk modulus of $K = 5 \times 10^4$ N/cm^2.

The petal geometry is discretised into 85 × 153 nodes in the domain of the $\theta - \phi$ coordinates specified in Eq. (57) that are then assembled into 798 25-noded spectral shell elements. These elements are equally distributed in the $\theta - \phi$ domain and therefore lead to finer spatial mesh densities towards the two ends of the petal. The growth deformation tensor $\boldsymbol{F}_g$ is defined with respect to a local Cartesian reference system that features two base vectors $\{\boldsymbol{e}_1, \boldsymbol{e}_2\}$ that lie in the plane of the petal with the third base vector $\boldsymbol{e}_3$ normal to the petal. The growth deformation tensor is isotropic in the plane and assumes no growth in the thickness direction. Hence, $\boldsymbol{F}_g(x, \lambda_g) = \text{diag}(g(x, \lambda_g), g(x, \lambda_g), 1)$, where $g(x, \lambda_g)$ is the planar growth function with greatest magnitude (parametrised through growth factor λ_g) at the edges of the petal ($x = \pm L_x/2$ cm) and smallest magnitude at the midrib ($x = 0$ cm). The growth function, inspired by measurements taken by Liang and Mahadevan [6], is assumed as

$$g(x, \lambda_g) = 1 + \lambda_g \left(\alpha + e^{\gamma(|x|-\beta)}\right), \tag{58}$$

where the exponential constant $\gamma = 4$, and the constants $\alpha = f_m - e^{-\gamma\beta}$ and $\beta = -\frac{1}{\gamma}\log\left(\frac{f_e - f_m}{e^{\gamma x_e} - 1}\right)$ are chosen to specify predefined values of the exponential term $f(x) = \alpha + e^{\gamma(|x|-\beta)}$ at the edges of the petal, *i.e.* $f(\pm L_x/2) = f_e$, and at the midrib of the petal, *i.e.* $f(0) = f_m$. The value at the edge of the petal is always defined as $f_e = 1$. To explore the effect of edge growth, we modulate the value at the midrib across the set $f_m \in \{0, 0.375, 0.75\}$. As $f_m \to 1$, the effect of differential edge grows diminishes such that we recover spatially uniform growth across the petal. Finally, the term $x_e = \sqrt{0.25L_x^2|1 - y^2/b^2|}$ used in the expression for β defines the x-location of the petal's edge, where b is the ellipsoid constant of Eq. (57). Hence, the growth function in Eq. (58) defines exponentially increasing growth magnitude in the width direction, with the greatest value of growth occurring along the curved petal edges and the smallest value of growth along the longitudinal midrib.

The equilibrium curves for the three cases $f_m \in \{0, 0.375, 0.75\}$, describing blooming of a single petal under edge growth, are shown in Fig. 15a. The equilibrium curves depict the evolution of the thickness-normalised z-axis displacement at the free tip of the petal (w/h) with increasing growth factor (λ_g). For all three cases, edge growth causes the tip of the petal to bend upwards, thereby reversing the original longitudinal curvature of the petal from

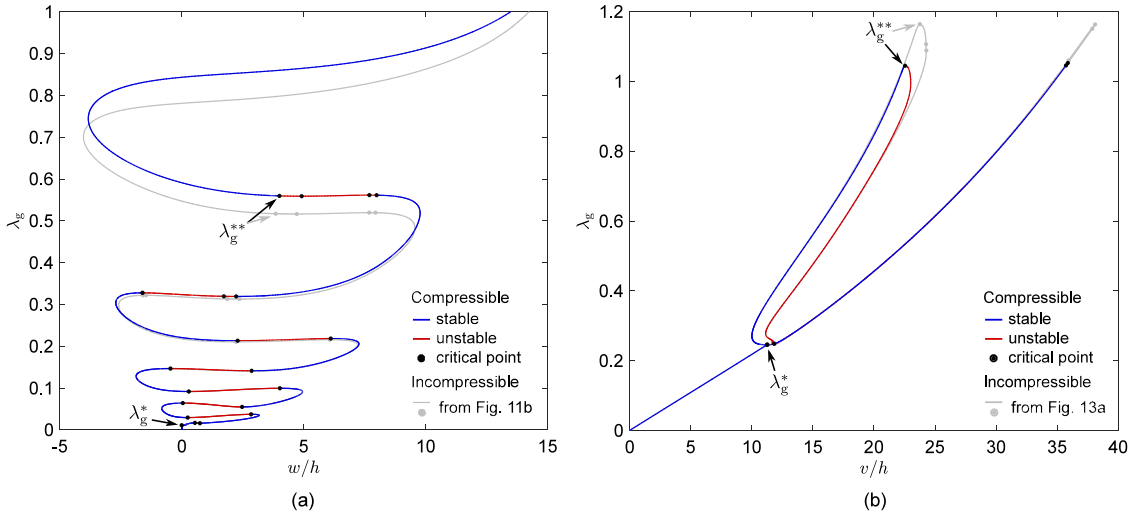

Fig. 16. Comparison of equilibrium manifold produced by the 'nearly' incompressible material model of Eq. (24) (grey curves) and the compressible Neo-Hookean material model of Eq. (59) (blue/red curves). (a) Exponential edge growth in *Asplenium scolopendrium*, originally modelled in Section 4.4. (b) Trumpeting and wrinkling of a daffodil corona, originally modelled in Section 4.5. (For interpretation of the references to colour in this figure legend, the reader is referred to the web version of this article.)

concave to convex. As shown for the intermediate value of $f_m = 0.375$ in Fig. 15b, the petal bends upwards from its original straight orientation to form a saddle shape that mimics the picture of the grown petal in Fig. 14b.

Beyond a certain threshold of growth, the z-axis displacement decreases again and this represents the tip of the petal rolling inwards onto itself (see point c in Fig. 15b). It is evident from Fig. 15a that the smaller the value of f_m, the smaller the value of λ_g for which this reversal of the tip z-displacement occurs. Hence, the more pronounced the degree of edge growth, *i.e.* the greater the difference between growth at the edges (f_e) and growth at the midrib (f_m), the less the absolute magnitude of growth required to induce blooming of the petal. For the case where $f_m \approx 1$ (not shown here), *i.e.* where growth is uniform across the petal, blooming does not occur at all; rather, the petal bends in the opposite direction (negative w/h), thereby increasing the original longitudinal concave curvature.

Spatially varying growth rates therefore play a key role in the blooming process of doubly-curved flower petals with greater levels of edge growth leading to more blooming action for the same level of added material. The concept of edge growth therefore provides an interesting mechanism for actuating morphing devices in engineering, which are often based on doubly-curved shells such as morphing chevrons for jet engine exhausts [69]. To date, these devices have relied on differential expansion through the thickness—as in a bi-metallic strip under thermal loading—but the insight into edge growth suggests that in-plane variations of chemical swelling or thermal expansion/contraction can also be used to facilitate morphing action.

5. Effect of material model and material parameters on pattern formation

In the literature, a variety of different material models are implemented to study thin biomaterials. In Section 2.4, one type of 'nearly' incompressible Neo-Hookean model was defined; see Eq. (24). We now assess the sensitivity of the post-critical results shown in Sections 4.4 and 4.5—*i.e.*, wrinkling of the fronds of hart's-tongue fern and trumpeting of a daffodil corona, respectively—to changes in the material model. All mesh characteristics, geometric dimensions, material parameters, and growth laws are kept unchanged.

As such, we modify the chosen material model to the compressible Neo-Hookean strain energy density:

$$\hat{W} = J_g W \quad \text{with} \quad W = \frac{\mu}{2}\left(\text{tr}\boldsymbol{C}_e - 3\right) - \mu \ln J_e + \frac{\lambda}{2}\left(\ln J_e\right)^2, \tag{59}$$

where μ is the shear modulus and λ is Lamé's first parameter, which is related to μ and the bulk modulus K through $\lambda = K - \frac{2}{3}\mu$. This leads to the usual second Piola–Kirchhoff stress and constitutive tensors covered in reference

Table 1
Comparison of the magnitude of specific critical points marked in Fig. 16 (to four sig. figs).

Critical point	'Nearly' incompressible	Compressible	$\|1-\lambda_g^{\text{comp}}/\lambda_g^{\text{incomp}}\|$
Fern λ_g^*	0.01093	0.01093	0%
Fern λ_g^{**}	0.5170	0.5596	8.24%
Daffodil λ_g^*	0.2457	0.2453	0.163%
Daffodil λ_g^{**}	1.164	1.045	10.2%

texts (*e.g.* [22]), with a scaling by J_g to account for changes in volume due to growth. Hence, the elastic second Piola–Kirchhoff stress tensor $\boldsymbol{S}_e$ and elastic constitutive tensor $\mathbb{D}_e$ are given by

$$\boldsymbol{S}_e = \mu J_g \left(\boldsymbol{I} - \boldsymbol{C}_e^{-1}\right) + \lambda J_g \ln J_e \boldsymbol{C}_e^{-1}, \tag{60}$$

$$\mathbb{D}_e = \lambda J_g \boldsymbol{C}_e^{-1} \otimes \boldsymbol{C}_e^{-1} + 2J_g \left(\lambda \ln J_e - \mu\right) \mathbb{I}_e, \tag{61}$$

with $\mathbb{I}_e$ defined in Eq. (32). These tensors are defined in the intermediate, stress-free configuration and therefore have to be pulled back to the original configuration via Eqs. (28) and (30), respectively.

The equilibrium manifolds of exponential edge growth in a frond of hart's-tongue fern (originally studied in Section 4.4) and the trumpeting and wrinkling of a daffodil corona (originally studied in Section 4.5) are compared in Fig. 16a and b, respectively. In each case, the equilibrium curve using the 'nearly' incompressible material model is shown as a grey trace, and the equilibrium curve using the compressible Neo-Hookean model is plotted as blue and red segments to denote stable and unstable equilibria, respectively.

For both examples considered, there are no qualitative changes in the post-critical pattern formation but visible quantitative differences in the equilibrium curves for increasing values of the growth factor λ_g. The two chosen material models both predict increasing number of wrinkles at the edges of the fronds of hart's-tongue fern as the growth factor λ_g increases (see deformation modes in Fig. 11c) with a back and forth winding equilibrium path. Similarly, both models predict the destabilisation of the trumpeting daffodil corona into nine full wrinkling waves (see deformation modes in Fig. 13d) at a supercritical pitchfork bifurcation. The increasing visible differences in the equilibrium curves for increasing growth parameter λ_g are supported by quantitative comparisons in Table 1 of specific critical points marked in Fig. 16a and b. In both plots, the critical point of the first bifurcation (λ_g^*) is almost identical between the 'nearly' incompressible and the compressible material models with negligible relative differences in magnitude (<0.2%). However, the relative differences increase to around 10% for critical points at greater magnitudes of growth (λ_g^{**}). Hence, there is a nonlinear quantitative effect to changing the material law from 'nearly' incompressible to compressible, and differences become more pronounced for increasing levels of growth. While these quantitative differences are important when comparing FE predictions to experiments or comparing results across different model formulations, it is important to note that the present examples suggest that the qualitative nature of the pattern formation in the post-critical regime is not strongly affected by the change in material model.

To further assess the effect of compressibility on post-critical pattern formation, we vary the bulk-to-shear moduli ratio K/μ in the compressible Neo-Hookean material model of Eq. (59) and study changes to the equilibrium manifold for exponential edge growth in hart's-tongue fern. The overall geometry, mesh properties, growth law and shear modulus are kept constant (same values as reported in Section 4.4) and only the bulk modulus is varied in the analyses. With decreasing K/μ, the relative compressibility of the material increases and Poisson's ratio decreases. As Fig. 16a showed that the equilibrium manifold is most affected in the high-magnitude growth range, *i.e.* in the deep post-critical regime, we focus on portions of the equilibrium manifold with $0.475 < \lambda_g < 1$.

Fig. 17a compares the equilibrium manifold for the 'nearly' incompressible material model with bulk-to-shear moduli ratio $K/\mu = 100$, and the compressible material model with $K/\mu = 100$ and $K/\mu = 10$. Interestingly, the equilibrium curves do not change monotonically with compressibility. Focusing on the unstable segment in Fig. 17a, the compressible material results for $K/\mu = 100$ and $K/\mu = 10$ straddle the result of the 'nearly' incompressible material model. To investigate this phenomenon further, the bifurcation point λ_g^{**} marked in Fig. 17a is traced with respect to changes in the bulk-to-shear moduli ratio K/μ (compressible Neo-Hookean material model) using the critical point tracking capability (see Section 3.4). In this manner, expensive parametric studies that trace the entire

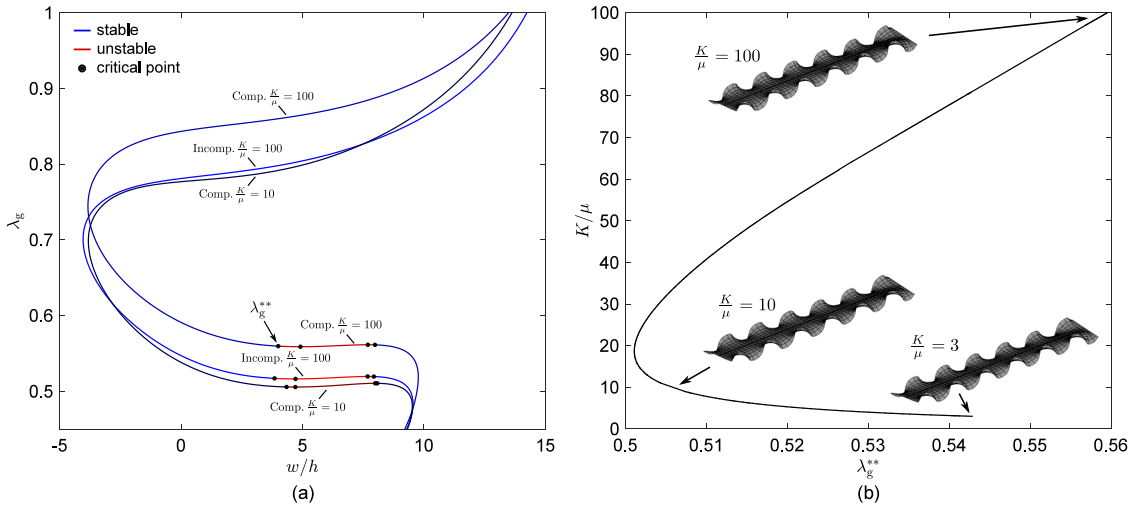

Fig. 17. (a) Comparison of the equilibrium manifold for exponential edge growth in *Asplenium scolopendrium* (originally modelled in Section 4.4) in the range $0.475 < \lambda_g < 1$. Results are shown for a 'nearly' incompressible material model with bulk-to-shear moduli ratio $K/\mu = 100$, and a compressible material model with $K/\mu = 100$ and $K/\mu = 10$. (b) Locus of the critical point λ_g^{**} marked in (a) with respect to changing bulk-to-shear moduli ratio K/μ for the compressible material model.

equilibrium manifold are precluded, and only one specific point is traced through parameter space by path-following a critical curve. Fig. 17b shows the evolution of λ_g^{**} with K/μ and confirms the non-monotonic relationship between the two quantities. For low compressibility (see $K/\mu = 100$), decreasing K/μ first leads to a reduction in λ_g^{**}, but for $K/\mu < 18.7$ the value of λ_g^{**} increases again. While Fig. 17b shows that the magnitude of λ_g^{**} can be affected by more than 10% for the specific problem and bulk-to-shear moduli ratios considered, the qualitative nature of the pattern formation is not altered. The post-critical wrinkling mode shapes at λ_g^{**} for three bulk-to-shear moduli ratios $K/\mu \in \{3, 10, 100\}$ all show six waves on both edges of the modelled leaf, arranged in an asymmetric left–right pattern (see Fig. 17b). This analysis illustrates the value of tracking critical curves through parameter space (*e.g.* uncertain material properties), both in terms quantifying changes to critical parameters as well as exploring any qualitative differences in pattern formation.

6. Conclusions

The aim of this paper is to present a robust modelling framework for growth-induced instabilities and associated geometrical pattern formation in growing systems. This is achieved by coupling a seven-parameter shell element to a hyperelastic material model and the decomposition of the deformation gradient tensor into a growth and an elastic part. The paper departs from previous work on computational analysis of morphoelastic instabilities by removing the need for seeding geometric, material or forcing perturbations into the model to bias the behaviour of a growing system onto a specific post-critical path. Instead, the stability characteristics of the growing biomaterial are tracked throughout the solution procedure, and when the number of eigenvalues of the tangent stiffness matrix changes, a critical pinpointing procedure is initiated to isolate the critical point. In the case of a branching bifurcation, branch switching to a connected equilibrium path can be initiated. In this manner, the post-critical stability and equilibrium landscape beyond the first (and any subsequent) instability can be robustly explored and pattern formation phenomena uncovered. This capability is especially useful for growing systems as multi-stability, *i.e.* the co-existence of multiple stable grown morphologies for the same level of growth, is the norm rather than the exception once a trivial fundamental state has lost stability.

The developed morphoelastic stability framework was applied to a diverse set of biologically inspired problems. In each of these cases, the central role of exponential edge growth—*i.e.*, spatially varying differential growth of exponentially increasing magnitude towards an edge—was highlighted. Depending on the precise parameters and characteristics of the growth law, exponential edge growth governs undulations at the edges of leaves (including fractal patterns over multiple length scales), the trumpeting and folding of a daffodil's corona, and the blooming

of doubly-curved flower petals. In addition, the morphoelastic stability framework allows a robust analysis of closely spaced as well as sequentially occurring bifurcations, which demonstrated the co-existence of multiple stable morphologies for the same level of growth magnitude and growth law. In these scenarios, small deviations in the initial conditions can mean that one stable morphology naturally evolves over a competing one. This mechanism of multi-stability could be an important factor governing the evolution of different morphologies in the same growing biomaterial for nearly identical starting conditions. It is precisely in this manner that the computational stability framework introduced here can help in advancing our understanding of the evolution of form and function in living systems, as well as aid in the development of bio-inspired engineering applications ranging from 4D printing and manufacturing of artificial tissues to morphing structures and active materials.

Declaration of competing interest

The authors declare that they have no known competing financial interests or personal relationships that could have appeared to influence the work reported in this paper.

Acknowledgement

This research is funded by the Royal Academy of Engineering, United Kingdom under the Research Fellowship scheme [Grant No. RF\201718\17178]. In addition, the author gratefully acknowledges the support of The Leverhulme Trust, United Kingdom through the Philip Leverhulme Prize.

Appendix A. First and second variations of the Green–Lagrange strain

From Eq. (19) the covariant components of the first variation of the Green–Lagrange strain are

$$\delta\epsilon_{\alpha\beta} = \frac{1}{2}\left[\delta\boldsymbol{v}_{,\alpha}\cdot\left(\bar{\boldsymbol{g}}_{\beta}+\boldsymbol{v}_{,\beta}\right)+\left(\bar{\boldsymbol{g}}_{\alpha}+\boldsymbol{v}_{,\alpha}\right)\cdot\delta\boldsymbol{v}_{,\beta}\right] \tag{A.1a}$$

$$\delta\kappa_{\alpha\beta} = \frac{h}{4}\left[\delta\boldsymbol{v}_{,\alpha}\cdot\left(\bar{\boldsymbol{n}}_{,\beta}+\boldsymbol{w}_{,\beta}\right)+\left(\bar{\boldsymbol{n}}_{,\alpha}+\boldsymbol{w}_{,\alpha}\right)\cdot\delta\boldsymbol{v}_{,\beta}+\delta\boldsymbol{w}_{,\alpha}\cdot\left(\bar{\boldsymbol{g}}_{\beta}+\boldsymbol{v}_{,\beta}\right)+\left(\bar{\boldsymbol{g}}_{\alpha}+\boldsymbol{v}_{,\alpha}\right)\cdot\delta\boldsymbol{w}_{,\beta}\right] \tag{A.1b}$$

$$\delta\epsilon_{\alpha 3} = \frac{h}{4}\left[\delta\boldsymbol{v}_{,\alpha}\cdot\left(\bar{\boldsymbol{n}}+\boldsymbol{w}\right)+\left(\bar{\boldsymbol{g}}_{\alpha}+\boldsymbol{v}_{,\alpha}\right)\cdot\delta\boldsymbol{w}\right] \tag{A.1c}$$

$$\delta\kappa_{\alpha 3} = \frac{h^2}{8}\left[\delta\boldsymbol{w}_{,\alpha}\cdot\left(\bar{\boldsymbol{n}}+\boldsymbol{w}\right)+\left(\bar{\boldsymbol{n}}_{,\alpha}+\boldsymbol{w}_{,\alpha}\right)\cdot\delta\boldsymbol{w}\right]+\frac{h}{2}\left[\left(\bar{\boldsymbol{g}}_{\alpha}+\boldsymbol{v}_{,\alpha}\right)\cdot\delta\boldsymbol{\Psi}+\delta\boldsymbol{v}_{,\alpha}\cdot\boldsymbol{\Psi}\right] \tag{A.1d}$$

$$\delta\epsilon_{33} = \frac{h^2}{4}\left(\bar{\boldsymbol{n}}+\boldsymbol{w}\right)\cdot\delta\boldsymbol{w} \tag{A.1e}$$

$$\delta\kappa_{33} = \frac{h^2}{2}\left[\left(\bar{\boldsymbol{n}}+\boldsymbol{w}\right)\cdot\delta\boldsymbol{\Psi}+\delta\boldsymbol{w}\cdot\boldsymbol{\Psi}\right], \tag{A.1f}$$

where $\delta\boldsymbol{\Psi} = (\delta\Psi)\bar{\boldsymbol{n}}$. Further, the second variation is given by

$$\Delta(\delta\epsilon)_{\alpha\beta} = \frac{1}{2}\left[\delta\boldsymbol{v}_{,\alpha}\cdot\Delta\boldsymbol{v}_{,\beta}+\Delta\boldsymbol{v}_{,\alpha}\cdot\delta\boldsymbol{v}_{,\beta}\right] \tag{A.2a}$$

$$\Delta(\delta\kappa)_{\alpha\beta} = \frac{h}{4}\left[\delta\boldsymbol{v}_{,\alpha}\cdot\Delta\boldsymbol{w}_{,\beta}+\Delta\boldsymbol{w}_{,\alpha}\cdot\delta\boldsymbol{v}_{,\beta}+\delta\boldsymbol{w}_{,\alpha}\cdot\Delta\boldsymbol{v}_{,\beta}+\Delta\boldsymbol{v}_{,\alpha}\cdot\delta\boldsymbol{w}_{,\beta}\right] \tag{A.2b}$$

$$\Delta(\delta\epsilon)_{\alpha 3} = \frac{h}{4}\left[\delta\boldsymbol{v}_{,\alpha}\cdot\Delta\boldsymbol{w}+\Delta\boldsymbol{v}_{,\alpha}\cdot\delta\boldsymbol{w}\right] \tag{A.2c}$$

$$\Delta(\delta\kappa)_{\alpha 3} = \frac{h^2}{8}\left[\delta\boldsymbol{w}_{,\alpha}\cdot\Delta\boldsymbol{w}+\Delta\boldsymbol{w}_{,\alpha}\cdot\delta\boldsymbol{w}\right]+\frac{h}{2}\left[\Delta\boldsymbol{v}_{,\alpha}\cdot\delta\boldsymbol{\Psi}+\delta\boldsymbol{v}_{,\alpha}\cdot\Delta\boldsymbol{\Psi}\right] \tag{A.2d}$$

$$\Delta(\delta\epsilon)_{33} = \frac{h^2}{4}\Delta\boldsymbol{w}\cdot\delta\boldsymbol{w} \tag{A.2e}$$

$$\Delta(\delta\kappa)_{33} = \frac{h^2}{2}\left[\Delta\boldsymbol{w}\cdot\delta\boldsymbol{\Psi}+\delta\boldsymbol{w}\cdot\Delta\boldsymbol{\Psi}\right]. \tag{A.2f}$$

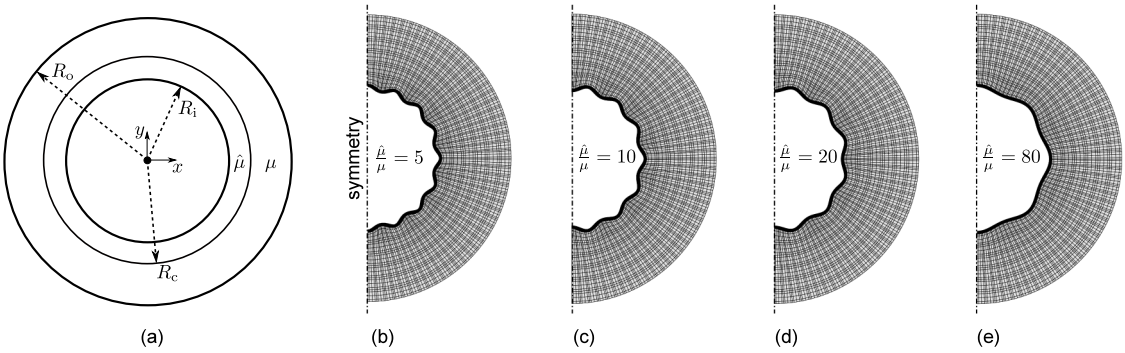

Fig. B.1. (a) A bilayer annulus with a growing inner layer and a non-growing outer layer that is clamped at the outer radius R_o. (b)–(e) Depending on the shear moduli ratio $\frac{\hat{\mu}}{\mu}$, the inner layer wrinkles into different number of waves. Following Jin et al. [60], only half of the domain is modelled herein.

Table B.1
Comparison of the critical growth factor (λ_g^*) and number of full waves (N_w) in the critical wrinkling eigenvector of the present stability framework and the results reported by Jin et al. [60].

$\frac{\hat{\mu}}{\mu}$	λ_g^* from [60]	λ_g^*	N_w from [60]	N_w
5	0.183	0.183	16	16
10	0.113	0.113	14	14
20	0.0699	0.0703	12	12
80	0.0272	0.0277	8	8

Appendix B. Validation of bifurcation analysis

Following the example of Jin et al. [60], we study planar buckling of an incompressible bilayer annulus subjected to isotropic planar growth of the inner layer only. As shown in Fig. B.1a, an annulus of outer radius $R_o = 1$, inner radius $R_i = 0.48$ and central interface radius $R_c = 0.5$ is considered with various ratios of shear moduli between the inner layer ($\hat{\mu}$) and the outer layer (μ). The inner layer is subjected to isotropic planar growth of $\boldsymbol{G}(\lambda_g) = (1+\lambda_g)\boldsymbol{g}_r \otimes \boldsymbol{g}_r + (1+\lambda_g)\boldsymbol{g}_\theta \otimes \boldsymbol{g}_\theta + 1\boldsymbol{g}_z \otimes \boldsymbol{g}_z$ expressed in a radial-azimuthal-transverse coordinate system, while the outer layer does not grow. Due to differential growth and the curvature of the domain, the inner layer wrinkles at a specific threshold value λ_g^* of the growth parameter.

The inner and outer layers of the annulus are both discretised into 6×50 radial-azimuthal 25-noded seven-parameter shell elements. Following Jin et al. [60], only half of the domain is modelled with symmetry conditions applied (see Fig. B.1b–e) and the outer radius of the annulus is rigidly clamped. To apply a plane strain condition in the transverse z-direction, all nodes are constrained in their out-of-plane displacement and thickness-stretch variables (v_z and Ψ, respectively). The thickness of the shell is defined to take an arbitrary value of $h = 1$. Four different shear moduli ratios $\frac{\hat{\mu}}{\mu} \in [5, 10, 20, 80]$ are modelled with the bulk moduli of the inner and outer layers equal to $1000\times$ their respective shear moduli.

The path-following solver is started from $\lambda_g = 0$ by increasing the value of the growth parameter until the number of negative eigenvalues in the tangent stiffness matrix changes to a non-zero value. At this point, the quadratically convergent bifurcation solver of Section 3.3 is initiated and the critical point determined. The four critical growth parameters λ_g^* for $\frac{\hat{\mu}}{\mu} \in [5, 10, 20, 80]$ are compared against the reported values of Jin et al. [60] in Table B.1 and all show excellent agreement. In addition, the number of waves N_w present in the corresponding critical eigenvector match those reported by Jin et al. [60]. The deformation modes of the critical eigenvectors are also shown on the modelled half-domain in Fig. B.1b–e.

References

[1] A. Goriely, The Mathematics and Mechanics of Biological Growth, Springer-Verlag, New York, USA, 2017.

[2] A.B. Tepole, C.J. Ploch, J. Wong, A.K. Gosain, E. Kuhl, Growing skin: a computational model for skin expansion in reconstructive surgery, J. Mech. Phys. Solids 59 (2011) 2177–2190.
[3] M. Marder, E. Sharon, S. Smith, B. Roman, Theory of edges of leaves, Europhys. Lett. 62 (4) (2003) 498–504, http://dx.doi.org/10.1209/epl/i2003-00334-5.
[4] H. Liang, L. Mahadevan, The shape of a long leaf, Proc. Natl. Acad. Sci. USA 106 (52) (2009) 22049–22054, http://dx.doi.org/10.1073/pnas.0911954106.
[5] E. Sharon, M. Marder, H. Swinney, Leaves, flowers and garbage bags: Making waves, Am. Sci. 92 (2004) 254–261, http://dx.doi.org/10.1511/2004.47.932.
[6] H. Liang, L. Mahadevan, Growth, geometry, and mechanics of a blooming lily, Proc. Natl. Acad. Sci. USA 108 (14) (2011) 5516–5521, http://dx.doi.org/10.1073/pnas.1007808108.
[7] S. Budday, P. Steinmann, E. Kuhl, The role of mechanics during brain development, J. Mech. Phys. Solids 72 (2014) 75–92.
[8] E. Kuhl, Unfolding the brain, Nature Physics 12 (2016) 533–534.
[9] D.E. Moulton, A. Goriely, Circumferential buckling instability of a growing cylindrical tube, J. Mech. Phys. Solids 59 (3) (2011) 525–537.
[10] P. Ciarletta, V. Balbi, E. Kuhl, Pattern selection in growing tubular tissues, Phys. Rev. Lett. 113 (2014) 248101.
[11] J.N. Wilking, V. Zaburdaev, M. De Volder, R. Losick, M.P. Brenner, D.A. Weitz, Liquid transport facilitated by channels in bacillus subtilis biofilms, Proc. Natl. Acad. Sci. USA 110 (3) (2013) 848–852.
[12] M. Trejo, C. Douarche, V. Bailleux, C. Poulard, S. Mariot, C. Regeard, E. Raspaud, Elasticity and wrinkled morphology of Bacillus subtilis pellicles, Proc. Natl. Acad. Sci. USA 110 (6) (2013) 2011–2016.
[13] A. Greiner, S. Kaessmair, S. Budday, Physical aspects of cortical folding, Soft Matter 17 (5) (2021) 1210–1222.
[14] H. Alawiye, E. Kuhl, A. Goriely, Revisiting the wrinkling of elastic bilayers I: linear analysis, Philos. Trans. A 377 (2019) 20180076.
[15] H. Alawiye, P.E. Farrell, A. Goriely, Revisiting the wrinkling of elastic bilayers II: Post-bifurcation analysis, J. Mech. Phys. Solids 143 (2020) 104053.
[16] D.-Y. Khang, J.A. Rogers, H.H. Lee, Mechanical buckling: mechanics, metrology, and stretchable electronics, Adv. Funct. Mater. 19 (2009) 1526–1536.
[17] J.B. Kim, P. Kim, N.C. Pégard, S.J. Oh, C.R. Kagan, J.W. Fleischer, H.A. Stone, Y.-L. Loo, Wrinkles and deep folds as photonic structures in photovoltaics, Nat. Photonics 6 (2012) 327–332.
[18] E.K. Rodriguez, A. Hoger, A.D. McCulloch, Stress-dependent finite growth in soft elastic tissues, J. Biomech. 27 (4) (1994) 455–467, http://dx.doi.org/10.1016/0021-9290(94)90021-3.
[19] L.A. Taber, Biomechanics of growth, remodeling, and morphogenesis, Appl. Mech. Rev. 48 (8) (1995) 487–545.
[20] E. Kuhl, Growing matter: A review of growth in living systems, J. Mech. Behav. Biomed. Mater. 29 (2014) 529–543, http://dx.doi.org/10.1016/j.jmbbm.2013.10.009.
[21] G.A. Holzapfel, Nonlinear Solid Mechanics: A Continuum Approach for Engineering, John Wiley & Sons, Chichester, England, 2000.
[22] P. Wriggers, Nonlinear Finite Element Methods, Springer-Verlag, Heidelberg, Germany, 2008.
[23] C. Kadapa, Z. Li, M. Hossain, J. Wang, On the advantages of mixed formulation and higher-order elements for computational morphoelasticity, J. Mech. Phys. Solids 148 (2021) 104289, http://dx.doi.org/10.1016/j.jmps.2020.104289.
[24] M. Ben Amar, A. Goriely, Growth and instability in elastic tissues, J. Mech. Phys. Solids 53 (2005) 2284–2319, http://dx.doi.org/10.1016/j.jmps.2005.04.008.
[25] A. Javili, P. Steinmann, E. Kuhl, A novel strategy to identify the critical conditions for growth-induced instabilities, J. Mech. Behav. Biomed. Mater. 29 (2014) 20–32, http://dx.doi.org/10.1016/j.jmbbm.2013.08.017.
[26] R.M.J. Groh, A. Pirrera, Extreme mechanics in laminated shells: New insights, Extreme Mech. Lett. 23 (2018) 17–23.
[27] Y. Klein, E. Efrato, E. Sharon, Shaping of elastic sheets by prescription of non-euclidean metrics, Science 315 (2007) 1116–1120.
[28] E. Sharon, E. Efrati, The mechanics of non-euclidean plates, Soft Matter 6 (2010) 5693–5704, http://dx.doi.org/10.1039/c0sm00479k.
[29] W.M. van Rees, E. Vouga, L. Mahadevan, Growth patterns for shape-shifting elastic bilayers, Proc. Natl. Acad. Sci. USA 114 (44) (2017) 11597–11602, http://dx.doi.org/10.1073/pnas.1709025114.
[30] E. Kuhl, A. Menzel, P. Steinmann, Computational modeling of growth, Comput. Mech. 32 (2003) 71–88.
[31] G. Himpel, E. Kuhl, A. Menzel, P. Steinmann, Computational modelling of isotropic multiplicative growth, Comput. Model. Eng. Sci. 8 (2005) 119–134.
[32] E. Kuhl, R. Maas, G. Himpel, A. Menzel, Computational modeling of arterial wall growth, Biomech. Model. Mechanobiol. 6 (2007) 321–331.
[33] D.P. Holmes, Elasticity and stability of shape-shifting structures, Curr. Opin. Colloid Interface Sci. 40 (2019) 118–137.
[34] J. Dervaux, M. Ben Amar, Morphogenesis of growing soft tissues, Phys. Rev. Lett. 101 (2008) 068101, http://dx.doi.org/10.1103/PhysRevLett.101.068101.
[35] J. Dervaux, P. Ciarletta, M. Ben Amar, Morphogenesis of thin hyperelastic plates: A constitutive theory of biological growth in the Föppl–von Kármán limit, J. Mech. Phys. Solids 57 (3) (2009) 458–471.
[36] M.K. Rausch, E. Kuhl, On the mechanics of growing thin biological membranes, J. Mech. Phys. Solids 63 (2014) 128–140.
[37] Y. Zheng, J. Wang, H. Ye, Y. Liu, H. Zhang, A solid-shell based finite element model for thin-walled soft structures with a growing mass, Int. J. Solids Struct. 163 (2019) 87–101, http://dx.doi.org/10.1016/j.ijsolstr.2018.12.024.
[38] S. Ahmad, B.M. Irons, O.C. Zienkiewicz, Analysis of thick and thin shell structures by curved finite elements, Int. J. Numer. Methods Eng. 2 (1970) 419–451.
[39] M. Bischoff, W.A. Wall, K.-U. Bletzinger, E. Ramm, Models and finite elements for thin-walled structures, in: E. Stein, R. de Borst, T.J.R. Hughes (Eds.), Encyclopedia of Computational Mechanics, John Wiley & Sons, 2004, pp. 59–137.

[40] N. Büchter, E. Ramm, Shell theory versus degeneration–a comparison in large rotation finite element analysis, Int. J. Numer. Methods Eng. 34 (1992) 39–59.
[41] E. Reissner, On the theory of bending of elastic plates, J. Math. Phys. 23 (1944) 184–191.
[42] J.C. Simo, D.D. Fox, On stress resultant geometrically exact shell model. Part I: formulation and optimal parametrization, Comput. Methods Appl. Mech. Engrg. 72 (1989) 267–304.
[43] M. Braun, M. Bischoff, E. Ramm, Nonlinear shell formulations for complete three-dimensional constitutive laws including composites and laminates, Comput. Mech. 15 (1994) 1–18.
[44] M. Bischoff, E. Ramm, Shear deformable shell elements for large strains and rotations, Int. J. Numer. Methods Eng. 40 (1997) 4427–4449.
[45] M. Büchter, E. Ramm, 3D-extension of nonlinear shell equations based on the enhanced assumed strain concept, in: C. Hirsch (Ed.), Computational Methods in Applied Sciences, Elsevier, Amsterdam, 1992, pp. 55–62.
[46] M. Bischoff, E. Ramm, On the physical significance of higher order kinematic and static variables in a three-dimensional shell formulation, Int. J. Solids Struct. 37 (2000) 6933–6960.
[47] E. Dvorkin, K.-J. Bathe, A continuum mechanics based four-node element for general non-linear analysis, Eng. Comput. 1 (1984) 77–88.
[48] J.C. Simo, M.S. Rifai, A class of mixed assumed strain methods and the method of incompatible modes, Int. J. Numer. Methods Eng. 29 (1990) 1595–1638.
[49] G.S. Payette, J.N. Reddy, A seven-parameter spectral/hp finite element formulation for isotropic, laminated composite and functionally graded shell structures, Comput. Methods Appl. Mech. Engrg. 278 (2014) 664–704, http://dx.doi.org/10.1016/j.cma.2014.06.021.
[50] D.J. Benson, Y. Bazilevs, M.-C. Hsu, T.J.R. Hughes, A large deformation, rotation-free, isogeometric shell, Comput. Methods Appl. Mech. Engrg. 200 (2011) 1367–1378.
[51] A. Javili, B. Dortdivanlioglu, E. Kuhl, C. Linder, Computational aspects of growth-induced instabilities through eigenvalue analysis, Comput. Mech. 56 (2015) 405–420, http://dx.doi.org/10.1007/s00466-015-1178-6.
[52] A. Papastavrou, P. Steinmann, E. Kuhl, On the mechanics of continua with boundary energies and growing surfaces, J. Mech. Phys. Solids 61 (2013) 1446–1463.
[53] P. Wriggers, J.C. Simo, A general procedure for the direct computation of turning and bifurcation points, Int. J. Numer. Methods Eng. 30 (1990) 155–176.
[54] V.A. Lubarda, A. Hoger, On the mechanics of solids with a growing mass, Int. J. Solids Struct. 39 (2002) 4627–4664, http://dx.doi.org/10.1016/S0020-7683(02)00352-9.
[55] A. Menzel, E. Kuhl, Frontiers in growth and remodeling, Mech. Res. Commun. 42 (2012) 1–14.
[56] A. Eriksson, Structural instability analyses based on generalised path-following, Comput. Methods Appl. Mech. Engrg. 156 (1998) 45–74.
[57] R.M.J. Groh, D. Avitabile, A. Pirrera, Generalised path-following for well-behaved nonlinear structures, Comput. Methods Appl. Mech. Engrg. 331 (2018) 394–426.
[58] G. Moore, A. Spence, The calculation of turning points of nonlinear equations, SIAM J. Numer. Anal. 17 (4) (1980) 567–576.
[59] W. Wagner, P. Wriggers, A simple method for the calculation of postcritical branches, Eng. Comput. 5 (1988) 103–109.
[60] L. Jin, Y. Liu, Z. Cai, Post-buckling analysis on growing tubular tissues: A semi-analytical approach and imperfection sensitivity, Int. J. Solids Struct. 162 (2019) 121–134.
[61] B. Audoly, A. Boudaoud, Self-similar structures near boundaries in strained systems, Phys. Rev. Lett. 91 (8) (2003) 086105, http://dx.doi.org/10.1103/PhysRevLett.91.086105.
[62] E. Sharon, B. Roman, H.L. Swinney, Geometrically driven wrinkling observed in free plastic sheets and leaves, Phys. Rev. E 75 (2007) 046211, http://dx.doi.org/10.1103/PhysRevE.75.046211.
[63] P.D. Woods, A.R. Champneys, Heteroclinic tangles in the unfolding of a degenerate Hamiltonian Hopf bifurcation, Phys. D 129 (1999) 147–170.
[64] R.M.J. Groh, A. Pirrera, On the role of localizations in buckling of axially compressed cylinders, Proc. R. Soc. A 475 (2019) 20190006.
[65] R.M.J. Groh, G.W. Hunt, A. Pirrera, Snaking and laddering in axially compressed cylinders, Int. J. Mech. Sci. 196 (2021) 106297.
[66] G.W. Hunt, R.M.J. Groh, T.J. Dodwell, Maxwell tipping points: the hidden mechanics of an axially compressed cylindrical shell, Proc. R. Soc. A 476 (2020) 20200273.
[67] J. Blahovec, Mechanical properties of some plant materials, J. Mater. Sci. 23 (1988) 3588–3593, http://dx.doi.org/10.1007/BF00540499.
[68] M. Eskandari, E. Kuhl, Systems biology and mechanics of growth, Wiley Interdiscip. Rev. Syst. Biol. Med. 7 (6) (2015) 401–412.
[69] J.H. Mabe, F.T. Calkins, G.W. Butler, Boeing's variable geometry chevron, morphing aerostructure for jet noise reduction, in: AIAA/ASME/ASCE/AHS/ASC Structures, Structural Dynamics and Materials Conference, Paper Nr. 2006-2142, Newport, RI, USA, 2006.